# SIMULATIONS OF VISCOUS ACCRETION FLOW AROUND BLACK HOLES IN A TWO-DIMENSIONAL CYLINDRICAL GEOMETRY

Seong-Jae Lee[1], Indranil Chattopadhyay[2], Rajiv Kumar[2], Siek Hyung[1], and Dongsu Ryu[3]
[1] School of Science Education (Astronomy), Chungbuk National University, Chungbuk 28644, Korea; seong@chungbuk.ac.kr
[2] ARIES, Manora Peak, Nainital-263002, Uttarakhand, India
[3] Department of Physics, School of Natural Sciences UNIST, Ulsan 44919, Korea

## ABSTRACT

We simulate shock-free and shocked viscous accretion flows onto a black hole in a two-dimensional cylindrical geometry, where initial conditions were chosen from analytical solutions. The simulation code used the Lagrangian total variation diminishing plus remap routine, which enabled us to attain high accuracy in capturing shocks and to handle the angular momentum distribution correctly. The inviscid shock-free accretion disk solution produced a thick disk structure, while the viscous shock-free solution attained a Bondi-like structure, but in either case, no jet activity nor any quasi-periodic oscillation (QPO)-like activity developed. The steady-state shocked solution in the inviscid as well as in the viscous regime matched theoretical predictions well. However, increasing viscosity renders the accretion shock unstable. Large-amplitude shock oscillation is accompanied by intermittent, transient inner multiple shocks. This oscillation of the inner part of the disk is interpreted as the source of QPO in hard X-rays observed in micro-quasars. Strong shock oscillation induces strong episodic jet emission. The jets also show the existence of shocks, which are produced as one shell hits the preceding one. The periodicities of the jets and shock oscillation are similar; the jets for the higher viscosity parameter appear to be stronger and faster.

*Key words:* accretion, accretion disks – hydrodynamics – instabilities – methods: numerical

## 1. INTRODUCTION

Investigation of the behavior of matter and radiation around black holes gained popularity when the accretion activity onto black holes became the only viable model to explain the power and spectra radiated by various active galactic nuclei (AGNs) and micro-quasars. Spectra around black hole candidates (BHCs) in both AGNs and micro-quasars show a thermal multi-colored component and non-thermal components. Some of these BHCs show only non-thermal spectra which can be fitted with the combination of one or two spectral indices, while others require a combination of thermal and non-thermal components. Moreover, most of these objects tend to be associated with relativistic jets, and observations indicate that these jets originate from within a few tens of Schwarzschild radii (Junor et al. 1999). Quasi-steady, mildly relativistic jets have been observed in the hard spectral state of the BHCs (Gallo et al. 2003); however, the jet power increases in transient outbursting objects, as they move from hard spectral states to intermediate states (Fender et al. 2004). Interestingly, the light curves of the stellar mass BHCs often show quasi-periodic oscillations (QPOs) of the hard photons (Miyamoto et al. 1992; Morgan et al. 1997; Remillard et al. 2002a, 2002b; Remillard & McClintock 2006; Nandi et al. 2012). Moreover, it has been shown that the evolution of spectral states, QPOs, and jet states can be expressed by a hysteresis-type hardness–intensity diagram (HID), or Q diagram, and many of the micro-quasars seem to follow this general pattern (Fender et al. 2004). It is to be noted that any model invoked to describe the accretion–ejection mechanism around BHCs should incorporate all of these issues.

Since the inner boundary condition for black hole accretion has to be supersonic, the first model of accretion onto a black hole was that of spherical radial inflow or relativistic Bondi accretion (Michel 1972). However, it was almost immediately pointed out that spherical accretion is too fast, and therefore that matter does not have enough time to produce the high luminosities that are observed outside the BHCs (Shapiro 1973a, 1973b). The focus then shifted to rotation-dominated disk models which are optically thick but geometrically thin and with negligible radial infall velocity. This disk model is called the Shakura–Sunyaev disk (SSD) or the Keplerian disk model (Novikov & Thorne 1973; Shakura & Sunyaev 1973). In spite of its simplicity, the Keplerian disk model explained the "big blue bump," or the modified blackbody part of the spectra from AGNs. However, there are some theoretical deficiencies in purely Keplerian disks, because the inner boundary of such a disk is too arbitrary, while the pressure gradient term is poorly understood. In addition, observationally the Keplerian disk cannot explain the presence of the hard power-law tail. It was understood that a hot component closer to the horizon could, in principle, scatter up the softer photons through an inverse-Compton process which would explain the observed hard power-law tail (Sunyaev & Titarchuk 1980). Since matter with non-negligible advection is also hotter, various models emerged, which have a significant advection term along with rotation.

Liang & Thompson (1980) showed that an inviscid, rotating accretion flow, which is a simpler form of advective flow, will have more than one sonic point. Such accretion flows with multiple sonic points may undergo shock transitions in both the inviscid and the viscous regime (Fukue 1987; Chakrabarti 1989, 1996).

Aside from the fixed-$\gamma$ equation of state of the flow, shocks have been obtained for flows with a variable-$\gamma$ equation of state as well (Fukue 1987; Chattopadhyay & Chakrabarti 2011; Kumar et al. 2013; Kumar & Chattopadhyay 2014). In the Paczyński–Wiita pseudo potential domain (Paczyński & Wiita 1980), accretion shocks were reported for various types of viscosity prescriptions, such as the Chakrabarti–Molteni type (Chakrabarti 1996), Shakura–Sunyaev type (Becker et al. 2008;

Kumar & Chattopadhyay 2013) and even for the causal viscosity type (Gu & Lu 2002). Accretion shocks were reported for general-relativistic viscous disks as well (Chattopadhyay & Kumar 2016).

However, the most popular model in the advective regime is the advection-dominated accretion flow (ADAF), which is characterized by a single sonic point close to the horizon, and is subsonic further out (Narayan et al. 1997). The ADAF, which was originally thought to be entirely subsonic and self-similar, was found to be self-similar only at large distances from the horizon (Chen et al. 1997). More interestingly, the ADAF has been proved to be a subset of a general advective solution (Lu et al. 1999; Becker et al. 2008; Kumar & Chattopadhyay 2013, 2014).

Since the entropy of the post-shock flow is higher, the accretion flow would undergo a shock transition whenever such a possibility arose, because nature favors a higher entropy solution. Shocks in accretion disks around black holes are advantageous. The post-shock disk (PSD) is hotter, slower, and denser than the pre-shock flow, although the density is not high enough to make the PSD optically thick. Hence, the PSD acts as a hot Comptonizing cloud that would produce the inverse-Comptonized hard power-law tail. The Comptonizing cloud obtained in this manner is not an arbitrary addition on the top of a disk solution, but arises naturally by solving the equations of motion in the advective regime, as will be shown in this paper. In a model solution, Chakrabarti & Titarchuk (1995) solved the radiative transfer equation for a two-component accretion flow, involving matter with high viscosity and Keplerian angular momentum distribution as well as sub-Keplerian matter. Matter with local Keplerian angular momentum occupies the equatorial plane and the sub-Keplerian flow sandwiches the Keplerian disk from the top and bottom. The sub-Keplerian flow, being hot and supersonic, experiences a shock transition, and as a result supplies hot electrons. The Keplerian disk supplies soft photons. The post-shock flow, being hot and puffed up, intercepts soft photons from the Keplerian disk, and inverse-Comptonizes them to produce the hard power-law tail as observed in the low-hard spectral state of the micro-quasars (Chakrabarti & Titarchuk 1995; Mandal & Chakrabarti 2010; Giri & Chakrabarti 2013). If the Keplerian accretion rate is increased beyond a critical limit, it cools down the PSD, creating what is known as the high-soft spectral state. Recent simulations show that this scenario is a distinct possibility (Giri & Chakrabarti 2013).

Interestingly, the PSD may or may not be stationary; it may be subject to a large number of instabilities. Since the PSD is hotter and denser, the cooling timescales may or may not be comparable with the dynamical timescale; where the two are comparable, the shock may oscillate (Molteni et al. 1996b; Okuda et al. 2007). And since the PSD produces the high energy power-law tail of the radiation spectrum, the oscillating shock should induce the same oscillation in hard photons—a very natural explanation of QPO in micro-quasars. Not only is the persistent oscillation or instability of the PSD related to the resonance between cooling and infall timescales, but viscosity might induce shock oscillations as well (Lanzafame et al. 1998; Lee et al. 2011; Das et al. 2014). There have been many stability studies of shocks (Nakayama 1992, 1994; Nobuta & Hanawa 1994; Gu & Foglizzo 2003; Gu & Lu 2006), but it has been shown that even under non-axisymmetric perturbations,

the shock tends to persist, albeit as a deformed shock (Molteni et al. 1999).

Apart from explaining the origin of hard power-law radiations and that of the QPO, the extra thermal gradient force in the PSD powers bipolar outflows. These outflows may be considered as precursor of jets (Molteni et al. 1994, 1996a, 1996b; Chattopadhyay & Das 2007; Okuda et al. 2007; Kumar & Chattopadhyay 2013). The HID for micro-quasars shows that as the micro-quasar enters the outbursting stage, both QPO and jet power increase while the spectral state evolves from low-hard to intermediate-hard/soft state (Fender et al. 2004; Radhika & Nandi 2014). Interestingly, since the post-shock region of the disk generates the outflow and shocks form close to the black hole, the observational constraint that a jet base is formed close to the horizon (Junor et al. 1999) is also satisfied. Recently, Kumar et al. (2014) showed that if the radiative acceleration of the shock-driven outflows are considered, then jet power increases as the spectral state of the disk moves from low-hard to intermediate-hard states, confirming the fact that has been observed (Fender et al. 2004).

Numerical simulations of accretion disks around black holes have been performed with codes based on smooth particle hydrodynamics (SPH), which has higher artificial viscosity (Molteni et al. 1994; Das et al. 2014), whereas others have been carried out with Eulerian codes (Molteni et al. 1996a; Nagakura & Yamada 2009; Okuda et al. 2007). Eulerian codes are based on upwind schemes and conserve energy and momentum naturally. So they efficiently capture and solve discontinuities like shock waves. However, in Eulerian schemes, azimuthal momentum is conserved but the angular momentum component is not. The SPH code, on the other hand, conserves angular momentum accurately in the absence of viscosity. Lee et al. (2011) developed a total variation diminishing (TVD) plus remap method, which combines the Lagrangian and TVD methods efficiently. With this Lagrangian TVD (LTVD) code, shocked accretion and ADAF-type solutions were accurately reproduced, and the code strictly conserves angular momentum in the inviscid scenario. Using the one-dimensional LTVD code, Lee et al. (2011) accurately reproduced theoretical accretion solutions, with strict conservation of angular momentum in inviscid flow. The introduction of viscosity creates a situation where the angular momentum redistributes and its dissipation becomes accentuated. As a result, beyond a critical value of viscosity the PSD starts to oscillate. Moreover, the possibility of forming multiple shocks, or the shock cascade conjectured by Fukumura & Tsuruta (2004), was also obtained by Lee et al. (2011), and shocks were observed to oscillate with separate, distinct frequencies.

In one-dimensional simulations, the dynamics in the vertical direction is suppressed. Therefore, the accretion–ejection phenomena cannot be investigated, because the ejection occurs in the vertical direction away from the equatorial plane. In this paper, we follow the methods of Lee et al. (2011) and perform multi-dimensional simulations of viscous accretion flow. Although shocks form for an inviscid accretion flow, is it possible to find steady shocks for a high viscosity parameter? Do multiple shocks form for multi-dimensional simulations, or is the phenomenon an artifact of one dimension? Moreover, earlier multi-dimensional simulations showed that the shock leaves the computational domain for higher viscosity (Lanzafame et al. 1998). The consensus reached was that, for

higher viscosity in the flow, shock withers away. In a one-dimensional simulation of Lee et al. (2011), the shock went out of the simulation box for high viscosity. However, in the one-dimensional analysis the dynamics along other directions is suppressed, therefore exaggerated dynamics along the relevant direction may force the shock to leave the computational domain. In this paper, we study the fate of the shock in multi-dimensional simulations for higher viscosity. In order to accommodate large-amplitude shock oscillations, we have chosen a larger computational box. Moreover, do the bipolar outflows from the PSD leave the computational domain with significant velocities in order to qualify these outflows as jet precursors? We address these issues in this paper. In Section 2, we present the governing equations. In Section 3, we describe the code and the tests performed to check the veracity of the code in multi-dimensions. In Section 4, we discuss the theoretical results and compare with simulations. In Section 5, we discuss the temporal behavior of a viscous accretion disk. In the last section, we present concluding remarks.

## 2. BASIC EQUATIONS

The mass, momentum, and energy conservation equations in two-dimensional cylindrical coordinates $(r, \theta, z)$ are given by

$$\frac{\partial \rho}{\partial t} + \frac{1}{r}\frac{\partial (r\rho v_r)}{\partial r} + \frac{\partial (\rho v_z)}{\partial z} = 0, \tag{1}$$

$$\frac{\partial (\rho v_r)}{\partial t} + \frac{1}{r}\frac{\partial (r\rho v_r^2)}{\partial r} + \frac{\partial (\rho v_r v_z)}{\partial z} + \frac{\partial P}{\partial r} = -\rho\frac{\partial \Phi}{\partial r} + \frac{\rho l^2}{r^3}, \tag{2}$$

$$\frac{\partial (\rho v_\theta)}{\partial t} + \frac{1}{r}\frac{\partial (r\rho v_\theta v_r)}{\partial r} + \frac{\partial (\rho v_\theta v_z)}{\partial z}$$
$$= \frac{1}{r^2}\frac{\partial}{\partial r}\left(\mu r^3 \frac{\partial \Omega}{\partial r}\right) + r\frac{\partial}{\partial z}\left(\mu\frac{\partial \Omega}{\partial z}\right), \tag{3}$$

$$\frac{\partial (\rho v_z)}{\partial t} + \frac{1}{r}\frac{\partial (r\rho v_r v_z)}{\partial r} + \frac{\partial (\rho v_z^2)}{\partial z} + \frac{\partial P}{\partial z} = -\rho\frac{\partial \Phi}{\partial z}, \tag{4}$$

$$\frac{\partial \bar{E}}{\partial t} + \frac{1}{r}\frac{\partial}{\partial r}(r\bar{E}v_r) + \frac{\partial}{\partial z}(\bar{E}v_z) + \frac{1}{r}\frac{\partial}{\partial r}(rPv_r) + \frac{\partial}{\partial z}(Pv_z)$$
$$= \frac{1}{r}\frac{\partial}{\partial r}\left(r^2\mu v_\theta \frac{\partial \Omega}{\partial r}\right) + \frac{\partial}{\partial z}\left(\mu v_\theta \frac{\partial v_\theta}{\partial z}\right) - \rho v_r\frac{\partial \Phi}{\partial r} - \rho v_z\frac{\partial \Phi}{\partial z}, \tag{5}$$

where, $\rho$, $v_r$, $v_\theta$, $v_z$, $l$, $\Phi$ and $\bar{E}$ are the gas density, radial velocity, azimuthal velocity, vertical velocity, specific angular momentum, gravitational potential, and total energy density, respectively. Here, $\bar{E} = \rho(v_r^2 + v_\theta^2 + v_z^2)/2 + \rho e$. Axis-symmetry is assumed. The angular velocity is defined as $\Omega = v_\theta/r = l/r^2$ and the pseudo-Newtonian gravity (Paczyński & Wiita 1980), assumed to mimic the Schwarzschild geometry, is given by:

$$\Phi = -\frac{GM_{\rm BH}}{R - r_{\rm g}}; \quad \text{where, } R = \sqrt{r^2 + z^2} \tag{6}$$

where $M_{\rm BH}$ is the black hole mass and the Schwarzschild radius is $r_{\rm g} = 2GM_{\rm BH}/c^2$. The gas pressure in the equation of state for an ideal gas is assumed,

$$P = (\gamma - 1)\rho e, \tag{7}$$

where $\gamma$ is the ratio of specific heats. Shakura & Sunyaev's viscosity prescription $(\alpha)$ is assumed, i.e., the dynamical viscosity coefficient is described by

$$\mu = \alpha\rho\frac{c_s^2}{\Omega_{\rm K}}, \tag{8}$$

where, the viscosity parameter $\alpha \leqslant 1$ is a constant. The square of the adiabatic sound speed is given by

$$c_s^2 = \frac{\gamma P}{\rho} \tag{9}$$

and

$$\Omega_{\rm K} = \frac{l_{\rm K}}{r^2} = \left[\frac{1}{r}\frac{\partial \Phi}{\partial r}\right]^{1/2} \tag{10}$$

is the Keplerian angular velocity. We have ignored cooling in this paper. We have assumed that only the $r - \theta$ component of the viscous stress tensor is significant.

In the following, $M_{\rm BH}$, $c$ and $r_{\rm g}$ are used as the units of mass, velocity, and length, respectively. Therefore, the unit of time is $t_{\rm g} = r_{\rm g}/c$. All of the equations, then, become dimensionless using the above unit system.

## 3. CODE

One of the most demanding tasks in carrying out numerical simulations of transonic flow is to capture shocks sharply. The upwind finite-difference schemes on an Eulerian grid have been known to achieve the shock capture strictly. However, since the angular momentum of Equations (1)–(5) is not treated as a conserved quantity in such Eulerian codes, we use the so-called LTVD scheme. The newly designed code can preserve the angular momentum perfectly because the Lagrangian concept is used, and it can also guarantee the sharp reproduction of discontinuities because the TVD scheme (Harten 1983; Ryu et al. 1993) is also applied (see Lee et al. 2011 for details). The calculation in the angular momentum transfer is updated through an implicit method, ensuring it is free from related numerical instabilities. However, the viscous heating without cooling is updated with a second-order explicit method, since it is subject to fewer numerical instabilities.

### 3.1. Hydrodynamic Part in a Multi-dimensional Geometry

We start with the hydrodynamic part in the Lagrangian step and remap, which consists of a plane-parallel and cylindrical geometry. The conservative form of Equations (1)–(5), in mass coordinates and in the Lagrangian grid, can be written as:

$$\frac{d\tau}{dt} - \frac{\partial (r^\alpha v)}{\partial m} = 0, \tag{11}$$

$$\frac{dv}{dt} + r^{\tilde{\alpha}}\frac{\partial p}{\partial m} = 0, \tag{12}$$

$$\frac{dl}{dt} = 0, \tag{13}$$

$$\frac{dE}{dt} + \frac{\partial (r^{\tilde{\alpha}}vp)}{\partial m} = 0, \tag{14}$$

where $\tau$ and $E$ are the specific volume and the specific total energy, respectively, related to the quantities used in
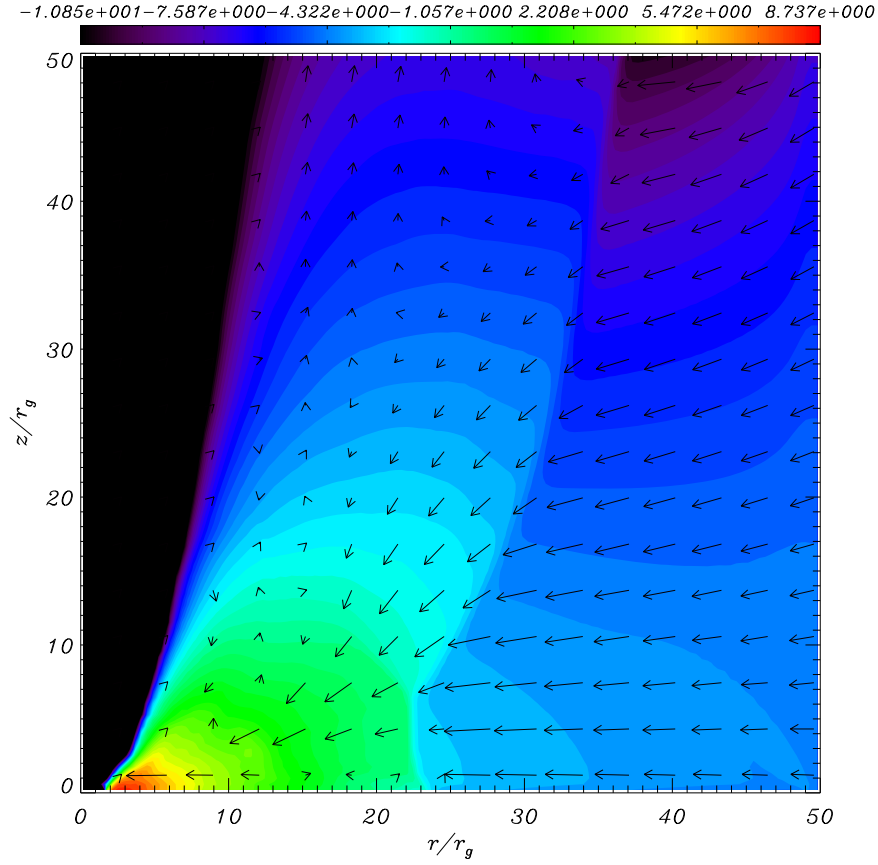
**Figure 1.** Density contours and velocity fields of a shocked accretion flow in the $r$–$z$ plane. The big paraboloidal accretion shock touches the equatorial plane at $r \sim 24 r_g$. The flow parameters are $v_{\rm rad} = -0.068212c$, $c_s = 0.061463c$, $\gamma = 4/3$, and $l = 1.65 r_g c$.

Equations (1)–(5) as

$$\tau = \frac{1}{\rho}, \qquad E = e + \frac{v^2}{2}. \qquad (15)$$

The mass coordinate related to the spatial coordinate is

$$dm = \rho(r) r^{\tilde{\alpha}} dr, \qquad (16)$$

and its position can be followed with

$$\frac{dr(z)}{dt} = v(m, t) \qquad (17)$$

where $\tilde{\alpha}$ represents the parameters in a different geometrical geometry; i.e., $\tilde{\alpha} = 0$ refers to the Cartesian coordinate system, while $\tilde{\alpha} = 1$ refers to the cylindrical geometry. Since Equations (11), (12), and (14) show a hyperbolic system of conservation equations, upwind schemes are applied to build codes that advance the Lagrangian step using Harten's TVD scheme (Harten 1983). Since the conserved Equations (1)–(5) are decomposed into a one-dimensional functioning code through a Strang-type directional splitting (Strang 1968) as in Ryu et al. (1995b), $\tilde{\alpha} = 1$ and $v = v_r$ and $\tilde{\alpha} = 0$ and $v = v_z$ are used for calculations along the $r$ and $z$ directions, respectively; $v_\theta$ is handled separately. Detailed explanations of the Lagrangian TVD and remap are given in Lee et al. (2011). Equation (13) does not need to be updated in the Lagrangian step since it is preserved in the absence of viscosity. Equations (1)–(5), calculated by the Lagrangian and remap steps, are updated in the Eulerian grid except for the centrifugal

force, gravity, and viscosity terms on the right-hand side. The centrifugal force in the $r$ direction only, and gravity terms in the $r$ and $z$ directions, are calculated separately after the Lagrangian and remap steps such that

$$v_i^{\rm hydro} = v_i^{\rm lag+remap} + \Delta t \left( \frac{l_i^{\rm remap}}{r_i^3} - \frac{d\Phi}{dr(z)} \Big|_i \right). \qquad (18)$$

Then the viscosity terms are calculated, as discussed in the following subsection.

### 3.2. Viscosity Part

Viscosity plays an important role in transferring angular momentum outward and it allows matter to accrete inward around a black hole. The angular momentum transfer in Equation (3) is described by the viscosity parameter given in Shakura & Sunyaev (1973).

Since the terms for the angular momentum transfer of radial and vertical directions in Equation (3) are linear in $l$, it is possible to calculate them implicitly. Substituting $(l^{\rm new} + l^{\rm remap})/2$ for $l$, Equation (3) without the advection term becomes

$$a_i' l_{i-1}^{\rm new} + b_i' l_i^{\rm new} + c_i' l_{i+1}^{\rm new} = - a_i' l_{i-1}^{\rm remap} - (b_i' - 2) l_i^{\rm remap} \\ - c_i' l_{i+1}^{\rm remap}, \qquad (19)$$

forming a tridiagonal matrix. Here $a_i'$, $b_i'$, and $c_i'$ are given with $\rho$, $\mu$, and $r$ as well as $\Delta r$ and $\Delta t$, while $a_i$, $b_i$, and $c_i$ are given
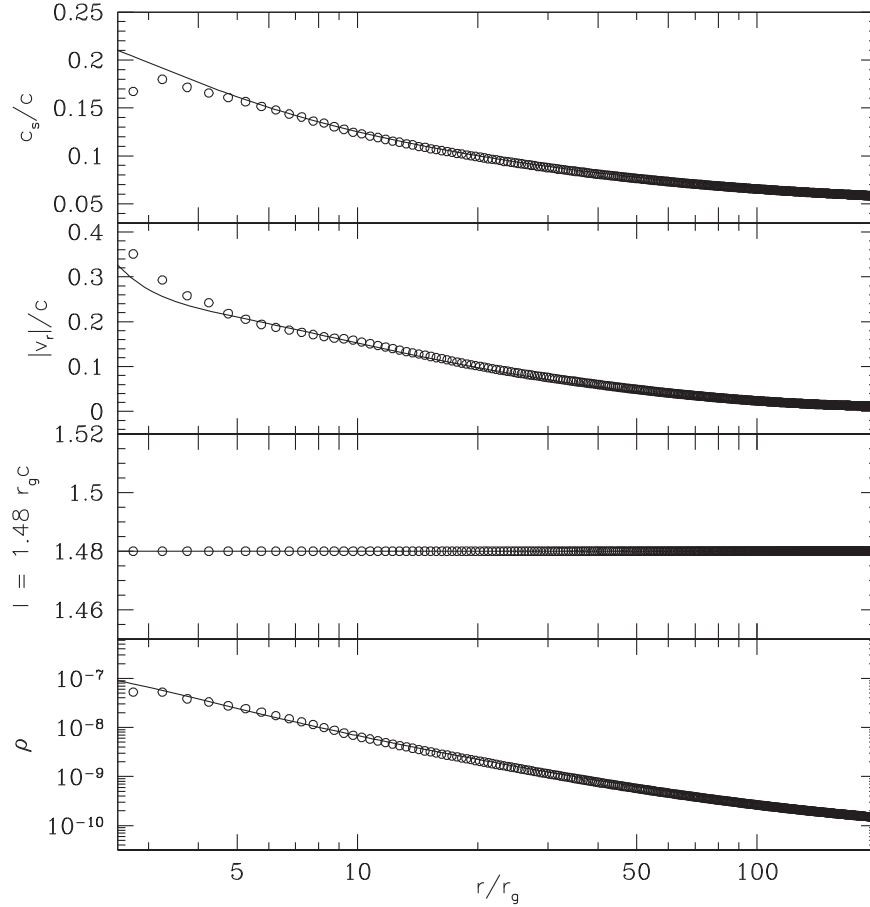
**Figure 2.** Test of the shock-free solution of case M1: $r_{inj} = 200\,r_g$, $v_r\,(\text{inj}) = -6.955509 \times 10^{-3}c$, $c_s\,(\text{inj}) = 5.9200845 \times 10^{-2}c$ and $l_{inj} = 1.48\,r_g c$. The solid lines represent the analytical solution, while the open circles represent the numerical solution. The adiabatic sound speed $c_s$, radial velocity $v_r$, specific angular momentum $l$, and density $\rho$ along the equatorial plane are shown from top to bottom.

with $\rho$, $\mu$, and $z$ as well as $\Delta z$ and $\Delta t$. The tridiagonal matrix is solved properly for $l^{new}$ with appropriate boundary conditions (Press et al. 1992). Another role of viscosity is to act as friction, resulting in viscous heating. Here, the viscous heating energy is fully saved as an entropy, since we ignore cooling. Our experience in dealing with numerical experiments tells us that the explicit treatment for the calculation of the viscous heating term does not cause any numerical problems. Thus angular momentum transfer is solved implicitly, while frictional heating energy is solved explicitly.

## 4. FORMATION OF SHOCKS IN A TWO-DIMENSIONAL GEOMETRY

### 4.1. Regeneration of a Two-dimensional Simulation Solution: A Test for the Code

We present a test result to demonstrate that the code can capture shocks sharply and resolve the structure clearly in a transonic flow. In the test, our result, in fact, corresponds to an earlier simulation result of Molteni et al. (1996a). The inviscid flow with the same initial conditions as in Molteni et al. (1996a) enters from the outer boundary, e.g., $v_{rad}\,(\text{inj})\,[\equiv \sqrt{v_r\,(\text{inj})^2 + v_z\,(\text{inj})^2}] = -0.068212c$, sound speed $c_s\,(\text{inj}) = 0.061463c$, adiabatic index $\gamma = 4/3$, and specific

angular momentum $l = 1.65\,r_g c$. The calculation in the cylindrical geometry was performed with $128 \times 256$ cells in a $50 \times 100\,r_g$ box size. Figure 1 clearly shows the presence of one shock structure along the equatorial plane, as seen in the result calculated using the SPH technique. Here the shock is resolved sharply as seen in the result calculated using the Eulerian TVD technique. Since the present code uses the Lagrangian scheme, in the absence of viscosity it can conserve angular momentum strictly. Hence, we can minimize the errors of the calculation of the specific angular momentum, present in a purely Eulerian scheme.

### 4.2. Theoretical Steady-state Solutions

So far, obtaining a proper time-dependent accretion solution around black holes is possible only through numerical simulations. However, early notions of the accretion–ejection paradigm emerged through theoretical efforts for semi-analytical solutions of the governing Equations (1)–(5) in the steady state (the so-called 1.5-dimensional analysis). These equations for the disk can be integrated to obtain the following constants of motion (Kumar & Chattopadhyay 2013), where the mass accretion equation is
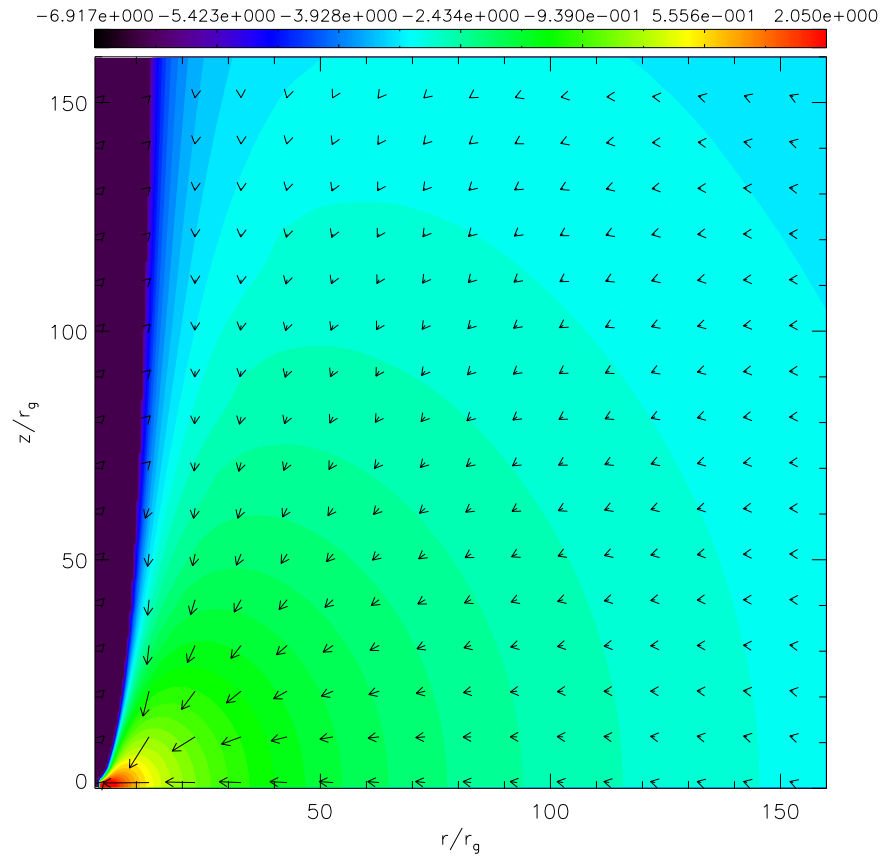
$$\dot{M} = 4\pi r H \rho v_r, \tag{20}$$

**Figure 3.** Density contour map and velocity field of the shock-free case M1.

and the specific energy, or the generalized Bernoulli parameter for viscous flow, is

$$\mathcal{E}_g = 0.5 v_r^2 + \frac{c_s^2}{(\gamma - 1)} - \frac{l^2}{2r^2} + \frac{l l_0}{r^2} + \Phi. \qquad (21)$$

Here $l_0$ is the specific angular momentum on the horizon—an integration constant, and $H = \sqrt{(2/\gamma)} \, c_s r^{1/2} (r - 1)$ is the local half-height of the accretion disk, assumed to be in hydrostatic equilibrium along the vertical direction. The gradient of the angular velocity obtained by integrating the azimuthal component of the Navier–Stokes equation as per the assumptions is given by

$$\frac{d\Omega}{dr} = -\frac{\gamma v_r \Omega_K (l - l_0)}{\alpha c_s^2 r^2}. \qquad (22)$$

It is very clear that in the absence of viscosity ($\alpha = 0$), $l = l_0$, and therefore, Equation (21) takes the usual form of the Bernoulli parameter $\mathcal{E} = \mathcal{E}_g = 0.5 v_r^2 + c_s^2/(\gamma - 1) + l_0^2/(2r^2) + \Phi$. Now for a given value of $\mathcal{E}_g$, $l_0$, and $\alpha$, the entire steady-state solution in the 1.5-dimensional analysis is obtained. In the rest of the paper we have assumed $\gamma = 1.4$, a value which will approximately describe electron–proton flow close to the horizon (Chattopadhyay & Ryu 2009; Chattopadhyay & Chakrabarti 2011; Kumar et al. 2013; Kumar & Chattopadhyay 2014). In this paper, we have used inviscid analytical solutions as initial conditions for viscous flow.

### 4.3. Comparison of Numerical Simulation with Theoretical Inviscid Solutions

Next we compare solutions obtained from our simulation code with analytical results of Kumar & Chattopadhyay (2013). We compare the shock-free and the shocked accretion solution. The accreting flow is supplied from the outer boundary which will be mostly absorbed at the inner edge of an accretion disk. The behavior of inviscid accreting matter around a black hole depends on the initial parameters of inflow, for instance its specific energy $\mathcal{E}$ and specific angular momentum $l_0$ (Kumar & Chattopadhyay 2013). As mentioned before, the theoretical steady-state solutions are obtained for a 1.5-dimensional analysis, i.e., a disk assumed to be in vertical hydrostatic equilibrium, while the simulation is done properly in two spatial dimensions. For $\gamma = 1.4$ and 1.5 dimensions, a steady-state shock solution exists for $1.5 r_g c < l_0 < 1.8 r_g c$ (for details, see Figure 2 of Kumar & Chattopadhyay 2013). We choose two analytical solutions from Kumar & Chattopadhyay (2013): model one, or M1, is a theoretical "shock-free" accretion solution with parameters, $l_0 = 1.48 r_g c$, and specific energy $\mathcal{E} = 0.0063 c^2$. The inflow variables at the injection radius $r_{inj} = 200 r_g$ are: $l_{inj} = 1.48 r_g c$, $v_r (inj) = -6.955509 \times 10^{-3} c$, $v_z (inj) = 0$, and $c_s (inj) = 5.920845 \times 10^{-2} c$. The computational box size is $200 r_g \times 200 r_g$ with a resolution of $400 \times 400$ cells.

Figure 2 compares simulation (open circles) with analytical (solid line) solutions, which represent sound speed, radial velocity, specific angular momentum, and density distribution along the equatorial plane from top to bottom. The simulation
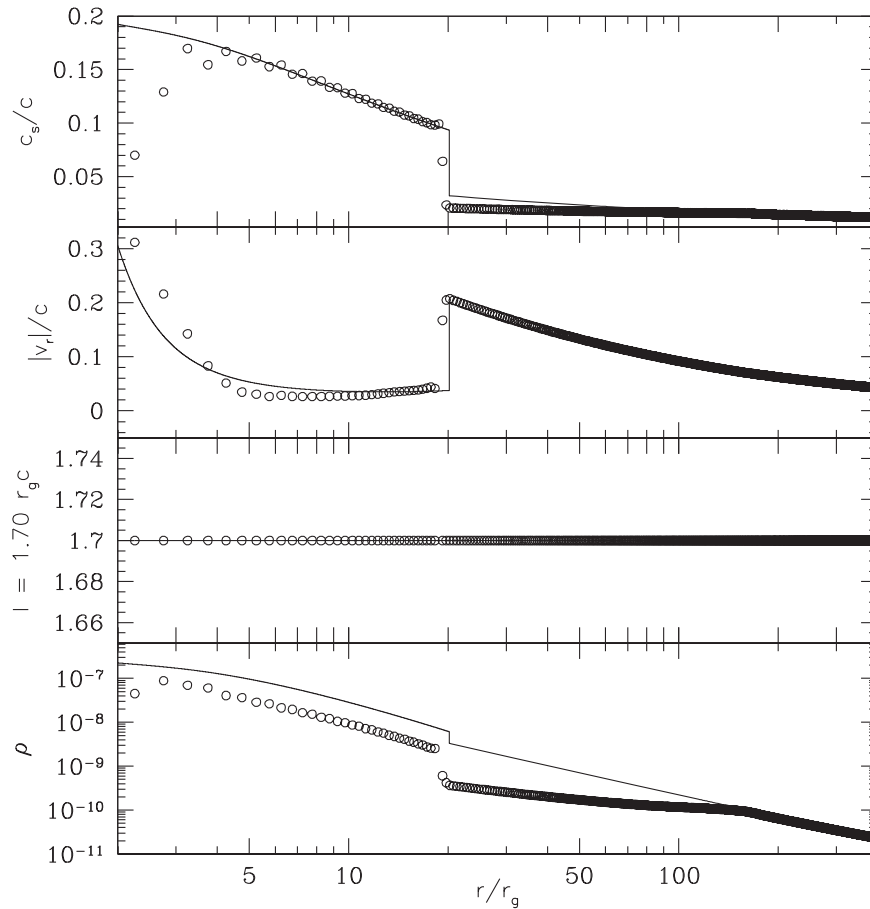
**Figure 4.** Case M2: the injection parameters here are the injection radius $r_{\mathrm{inj}} = 400 r_{\mathrm{g}}$, $v_r(\mathrm{inj}) = -4.249299 \times 10^{-2} c$, $c_s(\mathrm{inj}) = 1.190908 \times 10^{-2} c$, $l_{\mathrm{inj}} = 1.7 r_{\mathrm{g}} c$ and the height at $r_{\mathrm{inj}}$ is $H_{\mathrm{inj}} = 113.75\, r_{\mathrm{g}}$. The sound speed, velocity, specific angular momentum, and density are shown from top to bottom. The solid lines and open circles represent the analytical solutions and the numerical results, respectively. The analytical shock location is at $20.18\, r_{\mathrm{g}} c$, while the numerical one is at $19.25\, r_{\mathrm{g}} c$.

rigorously regenerates the analytical no-shock solution, once the steady state is reached. The agreement between the simulation and the analytical solution is remarkable. Close to the horizon, the flow falls very fast onto the black hole, so the vertical equilibrium assumption is not strictly maintained in those regions, causing a slight mismatch of $v_r$ and $c_s$ with the theoretical solution.

Figure 3 shows the density contour (color gradient) and velocity field (arrows) from the simulation of case M1 in the $r$–$z$ plane. Interestingly, the density contours mimic the thick disc configuration (Paczyński & Wiita 1980), although the advection term is significant in this simulation. We then simulate with injection parameters taken from Kumar & Chattopadhyay (2013), which predicts a theoretical shock in the inviscid limit, and we call this case M2. The parameters of M2 correspond to $\mathcal{E} = 1.25 \times 10^{-5} c^2$ and $l_{\mathrm{inj}} = 1.7 r_{\mathrm{g}} c$, with injection parameters $v_{\mathrm{rad}}(\mathrm{inj}) = -4.249299 \times 10^{-2}\, c$, $c_s(\mathrm{inj}) = 1.190908 \times 10^{-2}\, c$ at $r_{\mathrm{inj}} = 400 r_{\mathrm{g}}$. The height of the disc at $r_{\mathrm{inj}}$ is $H_{\mathrm{inj}} = 113.75 r_{\mathrm{g}}$.

Figure 4 shows the sound speed, radial velocity, specific angular momentum, and density distribution along the equatorial plane, which are plotted in panels from top to bottom, respectively. The solid lines show the analytical solution while the open circles show numerical results for the M2 case. The computational box size is $400 \times 200\, r_{\mathrm{g}}$ with $800 \times 400$ cells. The shock location from numerical calculations along the equatorial plane is about $19.25 r_{\mathrm{g}}$, while the

shock position suggested by the analytical solution is $20.18 r_{\mathrm{g}}$. The agreement of the theoretical solution (solid) with the numerical one (hollow circles) is fairly remarkable, for the simple reason that the numerical result is not restricted to no out-flow and vertical hydrostatic equilibrium, while the theoretical result is. Since hydrostatic equilibrium is, however, not well maintained close to the horizon, the shock location in the equatorial plane is slightly closer to the horizon than the theoretically predicted value indicates.

Figure 5 shows the snapshots of density contour and velocity field of case M2 at six time steps, showing how the solution progresses into the steady state. The first snapshot is for the time ($t = 10^3 t_{\mathrm{g}}$) when the accreting matter is still far away from the horizon. In the second and the third panels ($t = 3 \times 10^3 t_{\mathrm{g}}$ and $t = 4 \times 10^3 t_{\mathrm{g}}$), the injected matter has still not reached the horizon. The fourth ($t = 8 \times 10^4 t_{\mathrm{g}}$) and fifth ($t = 9 \times 10^3 t_{\mathrm{g}}$) panels show the formation of unsteady shocks with weak time-dependent post-shock outflows. The shock becomes steady at $t > 1.2 \times 10^4 t_{\mathrm{g}}$ as the solution reaches the steady state. Here, the density contours and velocity vectors are plotted for time $t = 2 \times 10^4 t_{\mathrm{g}}$. The inflow matter hits the effective potential barrier and is piled up behind it, where the accretion shock is formed. Earlier theoretical work already showed that there are two shock locations (Fukue 1987; Chakrabarti 1989) where the inner shock was found to be unstable while the outer one is stable (Nakayama 1992; Molteni et al. 1994). In our study, we also observe that the shock actually forms closer to the horizon,
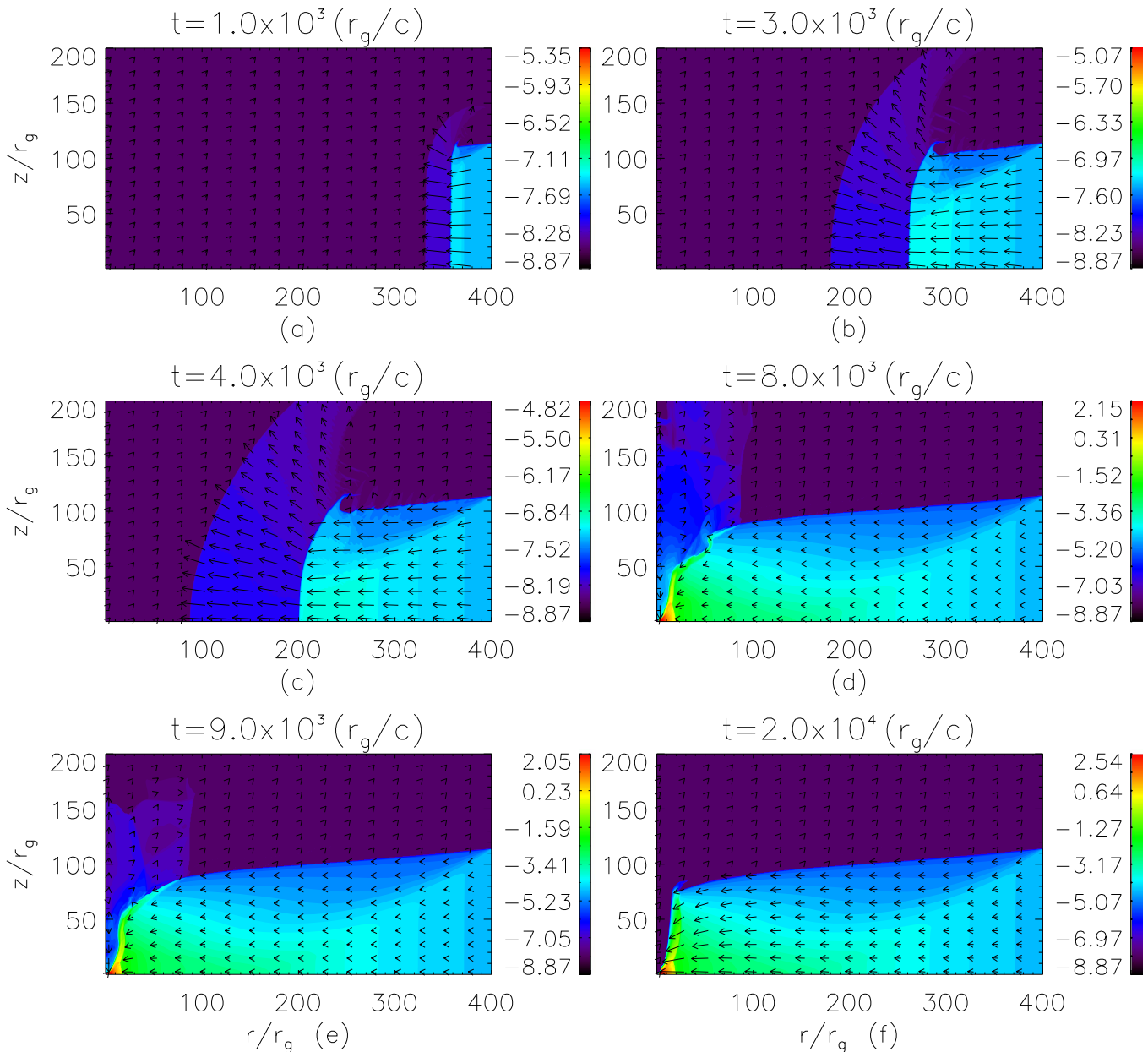
**Figure 5.** Density contours and velocity fields of a shocked inviscid disk. Six time steps (in units of dynamical time $t_g = r_g/c$) are plotted to show how the steady state is reached. The initial conditions are the same as in Figure 4.

but settles around the stable outer shock location once the steady state is reached. In the rest of the paper, we use the steady-state solution of M1 and M2 as the initial condition for the viscous flow.

## 5. SIMULATION OF VISCOUS FLOW

### 5.1. Steady-state Shock-free Disk

We turn on viscosity on the steady state of M1, or Figure 2. Viscosity transports angular momentum and, close to the horizon, the angular momentum greatly decreases and the disk morphology which represented that of the thick disk in the inviscid limit more resembles a Bondi flow. The flow direction is essentially spherical radial, as seen from the velocity vectors of Figure 6; once the steady state is reached, the density contours are almost spherical, corroborating a radial-type or

Bondi-type flow. The viscosity in this case is $\alpha = 0.05$, but we have also checked for $\alpha = 0.1$ and it remains a Bondi-type flow. No jet-like structure is seen, and no instability is seen which can be treated as a source of QPOs.

### 5.2. Steady-state Shocked Viscous Disk

In the next step, we include the viscosity terms in the aforementioned steady-state solution of M2. With small $\alpha$, the viscous solution remains stable, albeit for a different value of shock location, or $r_{sh}$. With the same injection parameters as those of the inviscid shocked flow, i.e., M2: $v_{rad}(\text{inj}) = -4.249299 \times 10^{-2} c$, $l_{inj} = 1.7 r_g c$ and $c_s(\text{inj}) = 1.190908 \times 10^{-2} c$ at $r_{inj} = 400 r_g$, we turn on the viscosity of $\alpha = 0.002$ at $t \sim 2.6 \times 10^4 t_g$. A theoretical solution with these injection parameters at $r_{inj} = 400 r_g$,
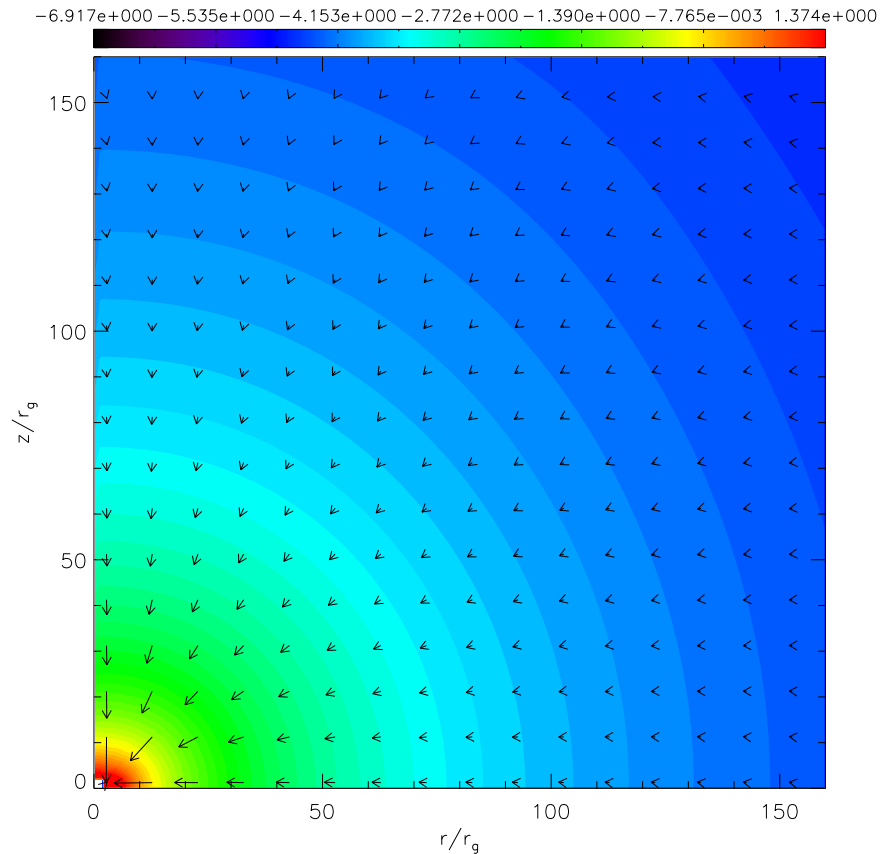
**Figure 6.** Density contours and velocity fields of a shock-free viscous disk for $\alpha = 0.05$. The initial conditions are the same as in Figure 2, or M1.

corresponds to a specific energy of $\mathcal{E}_g = 1.25 \times 10^{-5}\,c^2$ and $l_0 = 1.69966 r_g c$.

Figure 7 shows the corresponding global theoretical solution (solid lines) and the equatorial values of the simulation result (open circles). Top three panels show the distributions of $c_s$ in (a), $|v_r|$ in (b) and $l$ in (c), respectively, while Figure 7(d) shows the evolution of the equatorial shock location $r_{\rm sh}$ obtained from the simulation as a function of time. In the simulations, the steady shock location is at $r_{\rm sh} = 22.25 r_g$, while the theoretical shock is obtained at $22.45 r_g$. The position of $r_{\rm sh}$ moves out as viscosity is turned on. For low $\alpha$, the angular momentum transport between $r_{\rm inj}$ and $r_{\rm sh}$ is negligible, so in the pre-shock disk $l$ is roughly constant. It must be remembered, however, that if the computational box were increased to $10^5 r_g$, then the variation of angular momentum would have been discernible, as exhibited by the theoretical solution. Since the PSD is much hotter, the angular momentum transport is more efficient for the same value of $\alpha$. This causes the local angular momentum in the PSD to be greater than $l_{\rm inj}$. The extra centrifugal force therefore pushes the shock front outward. Figures 7(a)–(c) show the robustness of both the simulation and the analytical solution.

The PSD may eject outflows and experience turbulence, therefore some disagreement is inevitable between the analytical and simulation results. Moreover, since the vertical assumption does not hold well near the horizon, close to the horizon both $c_s$ and $v_r$ deviate from the analytical value. The angular momentum distribution of the simulation deviates from the analytical indication in the PSD region. However, the maximum fractional departure of the angular momentum distribution of the simulation from the analytically obtained

value is $\Delta l_{\rm sim}/l_{\rm analy} \lesssim 0.016$. Such a small degree of the deviation is within acceptable limits, considering that $r_{\rm sh}$ is reproduced quite accurately. We have plotted the analytical solution up to $r = 10^5 r_g$, in order to show that $r_{\rm inj}$ is not the actual outer boundary. Since the simulation for an eigenvalue solution like that of the accretion disk in a huge box of $10^5 r_g$ length scale is inconceivable or very expensive, we simulate the inner region of the disk. It is advisable that one should be careful in analyzing or addressing the outer boundary condition when the simulation box is only within the inner few hundred Schwarzschild radii.

Figure 8 displays snapshots of density contours and velocity vectors of the flow with the same initial and boundary conditions as in Figure 7, at various time steps (marked above the panels). These snapshots show that indeed the solution reaches the steady state at $t \gtrsim 4 \times 10^4 t_g$. For both the viscous and inviscid cases, the agreement between the theoretical/ semi-analytical solutions and the simulated solutions on the equatorial plane is fairly satisfactory given the fact that the analytical solutions are obtained under vertical equilibrium and no outflow assumptions, while the simulations are just time-dependent solutions of the fluid equations in two dimensions, where such assumptions are not implemented. As far as we know, the comparison of a theoretical solution and a simulated solution for a steady-state shock in the presence of viscosity was not undertaken to any great extent in earlier studies.

### 5.3. Shock Oscillation in a Disk

Shock oscillations have been observed in the presence of cooling (Molteni et al. 1996b; Okuda et al. 2007), for inviscid
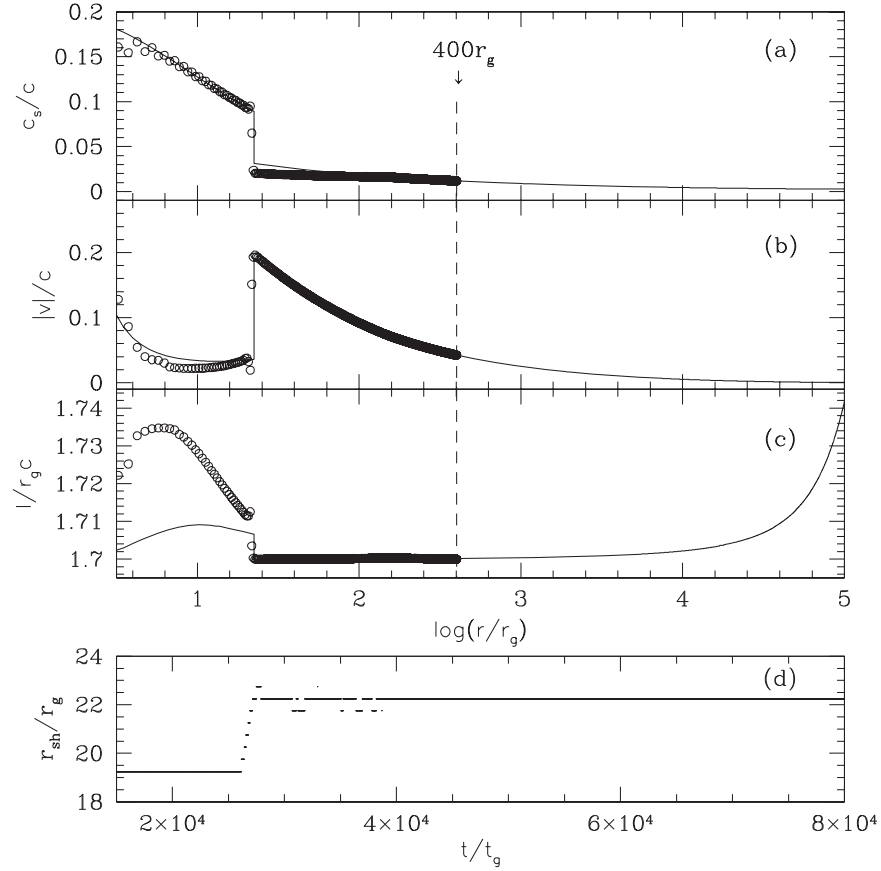
**Figure 7.** Comparison of the theoretical, vertical equilibrium model (solid lines), and the two-dimensional simulation results on the equatorial plane (open circles) of the viscous flow. The computation box is $200r_g \times 400r_g$ in the $r$–$z$ plane. The analytical solution is plotted up to $10^5 r_g$. The injected parameters are $v_r \text{(inj)} = -4.249299 \times 10^{-2}\,c$, $l_{inj} = 1.7 r_g c$, and $c_s \text{(inj)} = 1.190908 \times 10^{-2} c$ at $r_{inj} = 400 r_g$. The flow variables are $c_s$ in (a), $|v_r|$ in (b), and $l$ in (c). The locus of shock $r_{sh}$ with time (d), shows that $r_{sh}$ reaches the steady state after $t \gtrsim 4 \times 10^4 t_g$. The viscosity parameter is $\alpha = 0.002$. The vertical dashed line denotes $r_{inj}$.

and adiabatic flows and for Newtonian point mass gravity (Ryu et al. 1995a) or for stronger gravity (Ryu et al. 1997), also in the presence of viscosity (Lanzafame et al. 1998, 2008; Lee et al. 2011; Das et al. 2014). It has been generally accepted that accretion shocks may exist for low viscosity and cannot be sustained for $\alpha >$ few $\times 10^{-3}$ (Lanzafame et al. 1998, 2008). However, shocks may exist theoretically for $\alpha \lesssim 0.3$ (Kumar & Chattopadhyay 2013, 2014), which is fairly high. The flow parameters we have chosen for our simulation are in the domain where steady shocks do not exist for high $\alpha$. We would therefore like to find out whether oscillatory shocks exist for these injection parameters, or the shock completely fades away. With a one-dimensional LTVD code, we showed that persistent oscillatory shocks exist for $\alpha \sim$ few $\times 10^{-2}$ (Lee et al. 2011). Now we would like to investigate this scenario in multi-dimensions, since LTVD as a scheme is superior to both the TVD and Lagrangian codes.

As has been mentioned, the initial condition for the viscous flow is the steady state as in M2, and the boundary condition of M2 is also employed. In our study, we found that the steady-state shock tends to oscillate for $\alpha > 0.003$. Our results also show that a hotter PSD ensures higher average $l$ than that of the immediate pre-shock disk. This causes an outward centrifugal thrust which pushes $r_{sh}$ out. If this thrust is greater than the sum of ram pressure and the gas pressure of the pre-shock disk, then $r_{sh}$ will move out instead of settling down. However, the expanding $r_{sh}$ also causes a total pressure drop within the PSD.

This would restrict the outward motion trying to contract $r_{sh}$. Due to the competition between outward expansion and contraction, the $r_{sh}$ is in oscillation mode. In Figure 9, we plot $r_{sh}$ versus $t$ for (a) $\alpha = 0.003$, (b) 0.005, (c) 0.007 and (d) 0.01, respectively. The shock starts to oscillate as in Figure 9(a), and then undergoes close to a regular oscillation for higher $\alpha$ (b). In the case of higher $\alpha$, (c) and (d), the shock oscillation is no longer in regular mode and the amplitude of the oscillation increases.

Figure 10 shows snapshots of density contours and velocity field of an accretion solution for $\alpha = 0.01$. The time of each snapshot is mentioned in the figure. For $\alpha = 0.01$ the jets are observed to be episodic. The strength of the jet is clearly related to the dynamics of the PSD, but now multiple shocks appear. In order to show these, we plot $-v_r/c$ (Figures 11(a)–(d)), $c_s/c$ (Figures 11(e)–(h)) and $l/(r_g c)$ (Figures 11(i)–(l)), measured on the equatorial plane, at $t = 2.474 \times 10^5 t_g$ (Figures 11(a), (e), (i)), $t = 2.480 \times 10^5 t_g$ (Figures 11(b), (f), (j)), $t = 2.496 \times 10^5 t_g$ (Figures 11(c), (g), (k)) and $t = 2.508 \times 10^5 t_g$ (Figures 11(d), (h), (l)). Three shocks appear at $t = 2.480 \times 10^5 t_g$ (b, f, j): but the outer shock moves inward at $t = 2.480 \times 10^5 t_g$, while the inner shocks tend to collide, and ultimately one shock survives at $t = 2.508 \times 10^5 t_g$. The shock locations are marked by downward arrows for two epochs $t = 2.474 \times 10^5 t_g$ and $t = 2.480 \times 10^5 t_g$. This pattern occurs repeatedly. The jet off
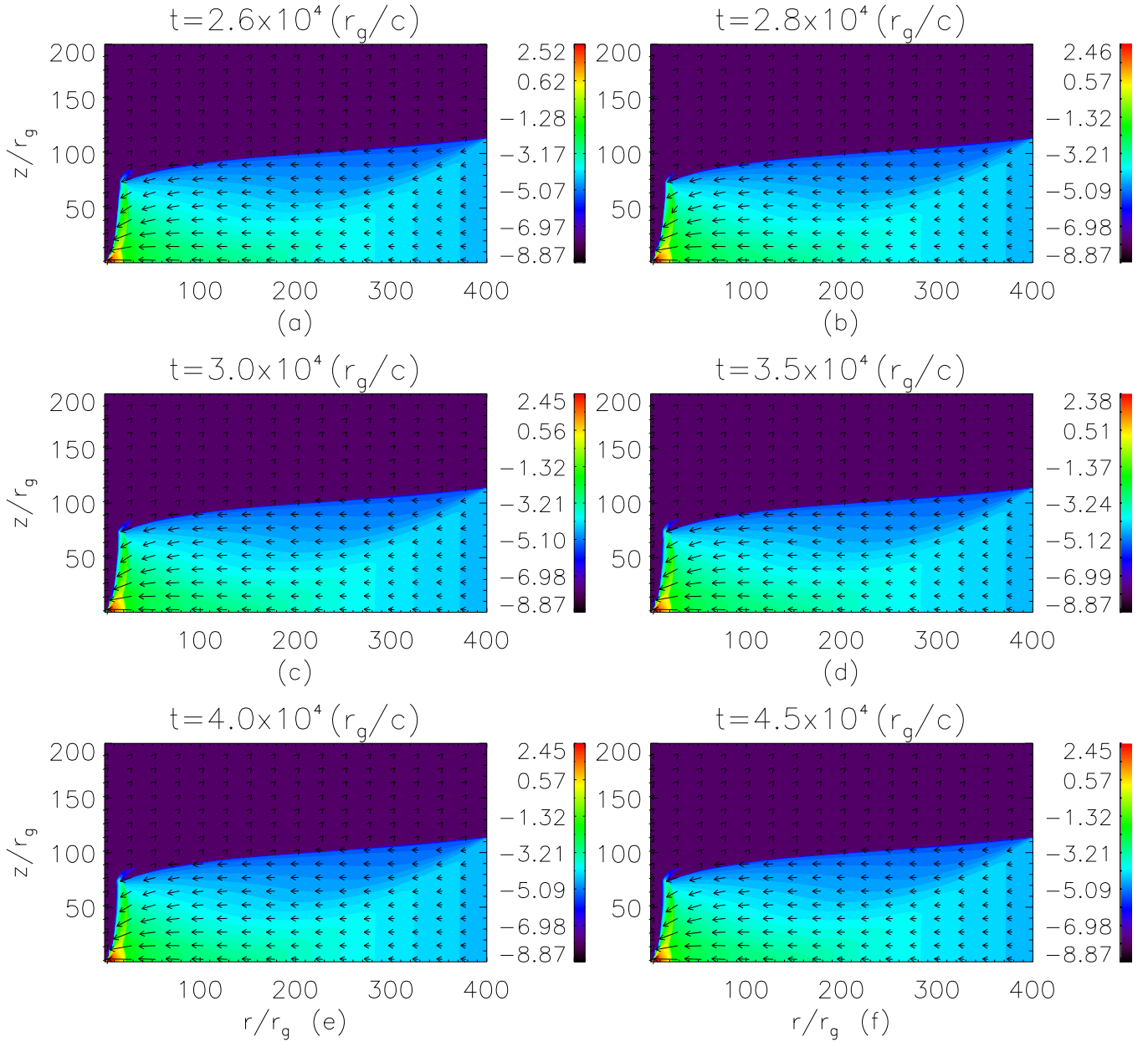
**Figure 8.** Density contours and velocity fields of a shocked viscous disk for the six time snapshots mentioned on each panel. The initial conditions are the same as in Figure 7.

state ($t = 2.508 \times 10^5 t_g$) is clearly seen in Figure 10(f), where the bipolar outflow perishes. All the snapshots of Figures 10 and 11 are from one episode of an oscillating shock starting from a high jet state to its declining state, and are shown in Figures 12(a)–(d) by two dashed vertical lines. Note that the episodic jet ejections do not constitute relativistic ballistic ejections, but rather these ejections result in a continuous stream of jet blobs which constitutes a quasi-steady jet. In order to quantify the mass outflow rate, we define

$$\dot{m}_{out} = \int \rho v_{out} \, dA \, \text{(outer edge)} \qquad (23)$$

and

$$\dot{m}_{inj} = \int \rho v_{inj} \, dA \, \text{(upto } H_{inj}), \qquad (24)$$

where $dA$ is the elemental surface area. The matter which is flowing with $v_z > 0$ and $v_r > 0$ at the outer edge of the computational box is considered as a jet. The relative outflow rate is

$$R_{\dot{m}} = \dot{m}_{out}/\dot{m}_{inj}. \qquad (25)$$

To see a simplified case of emissivity of these systems, we estimate the bremsstrahlung emission from the flow. The bremsstrahlung emissivity is $e_{Brem} \propto \rho^2 T^{1/2} \propto \rho^2 c_s$ (energy/volume/time). Therefore, the bremsstrahlung loss through each volume element, apart from constants and geometrical factors, is $\delta \epsilon_{Br} \propto e_{Brem} r^2 dr$. If the radiation is locally isotropic, i.e., equal fluxes in the three directions then, a third of $\delta \epsilon_{Br}$ escapes through the top surface (along $z$). One may be tempted to
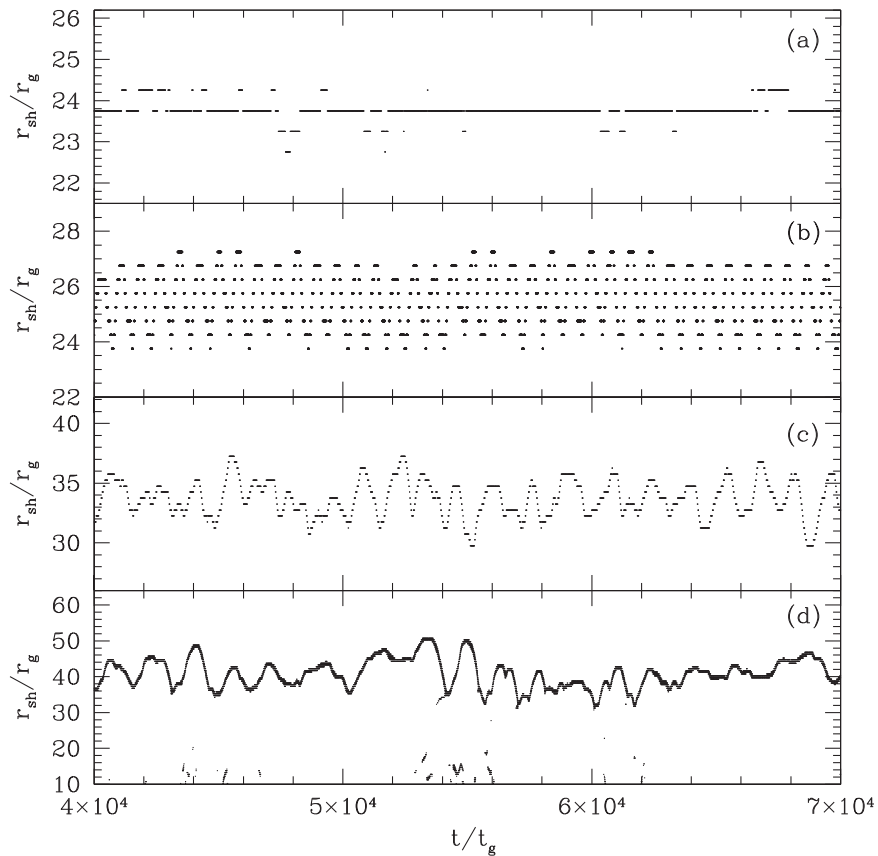
**Figure 9.** Shock location $r_{sh}$ vs. $t$. Each panel represents different viscosity, where (a) $\alpha = 0.003$, (b) $\alpha = 0.005$, (c) $\alpha = 0.007$, and (d) $\alpha = 0.01$. The boundary conditions are same as for M2 and the initial condition is the steady state of M2.

compare this with the factor of a half associated with energy loss from an SSD! The latter is an optically thick, geometrically thin disk with negligibly small advection. The viscous energy dissipated is converted into radiation which will be thermalized because the disk is optically thick, and since it is geometrically thin, the entire amount of radiation generated has to escape through the top and bottom surfaces, which brings in the factor of $1/2$. In contrast, an advective disk like the one simulated here, is neither optically thick nor geometrically thin, i.e., $H/r \lesssim 1$. Therefore, radiation will advect along the $r$ and $\theta$ directions as well as escaping along $z$. Therefore, in the absence of a proper radiative transfer treatment, we assume only a third of the radiation generated escapes along $z$ from the top half the disk. Due to the up–down symmetry assumed, the same is supposed to occur below the equatorial plane.

Then, the intensity ($I_0$) at each grid point is obtained by dividing $\delta\epsilon_{Br}/3$ by the top surface area of each volume. Special relativity implies that the radiative intensity in the observer frame will be $I = I_0/[\Gamma(1 - v_z)]^4$, where $I_0$ is the intensity in the comoving frame, and $\Gamma$ is the bulk Lorentz factor. This transformation is obtained by starting from the first principle that the phase space density of photons is Lorentz invariant and which has been shown by many authors (Hsieh & Spiegel 1976; Mihalas & Mihalas 1984; Kato et al. 1998). Moreover, depending on from where the radiation is emitted, a factor of $\mathcal{G}$ is to be taken into account to obtain the amount of the radiation eaten up by the black hole (Shapiro &

Teukolsky 1983; Vyas et al. 2015), where

$$\mathcal{G} = \frac{\pi - \sin^{-1}[3\sqrt{3}\,(1 - 1/R)/(2R)]}{\pi}; \quad R = \sqrt{(r^2 + z^2)}.$$
(26)

All these corrections are included in estimating the bremsstrahlung loss $\epsilon_{Br}$ at each time step. As the disc becomes unstable, the radiation emitted by the flow should exhibit the same fluctuation. While calculating $\epsilon_{Br}$, we express $e_{Brem}$ in units of $e_{Brem}$ at $r_{inj}$ to make the estimate bremsstrahlung loss dimensionless.

Figure 12(a) shows $r_{sh}$ with time for $\alpha = 0.01$, and Figure 12(b) shows $R_{\dot{m}}$ with time. In Figure 12(c), we plot the estimated bremsstrahlung loss $\epsilon_{Br}$ integrated up to $H_{inj}$, while in Figure 12(d) we plot the shock speed in the black hole rest frame with time. Figures 10 and 11 correspond to various time snapshots within the marked region of Figures 12(a)–(d). The mass outflow rate is episodic; as the shock generally expands from a minimum, the PSD loses its upward thrust, reducing $R_{\dot{m}}$. As $r_{sh}$ moves inward, it squeezes more matter out and $R_{\dot{m}}$ increases. We also notice the occurrence of intermittent inner shocks in Figure 12(a). These secondary shocks are not predicted analytically, but only witnessed numerically. It is instructive to note that the radiative loss follows a time series pattern which has an oscillatory period similar to that of the oscillating shock. The shock speed versus time plot shows that the shock speed is generally an order of magnitude smaller than the local sound speed and the dynamical speed in the post-
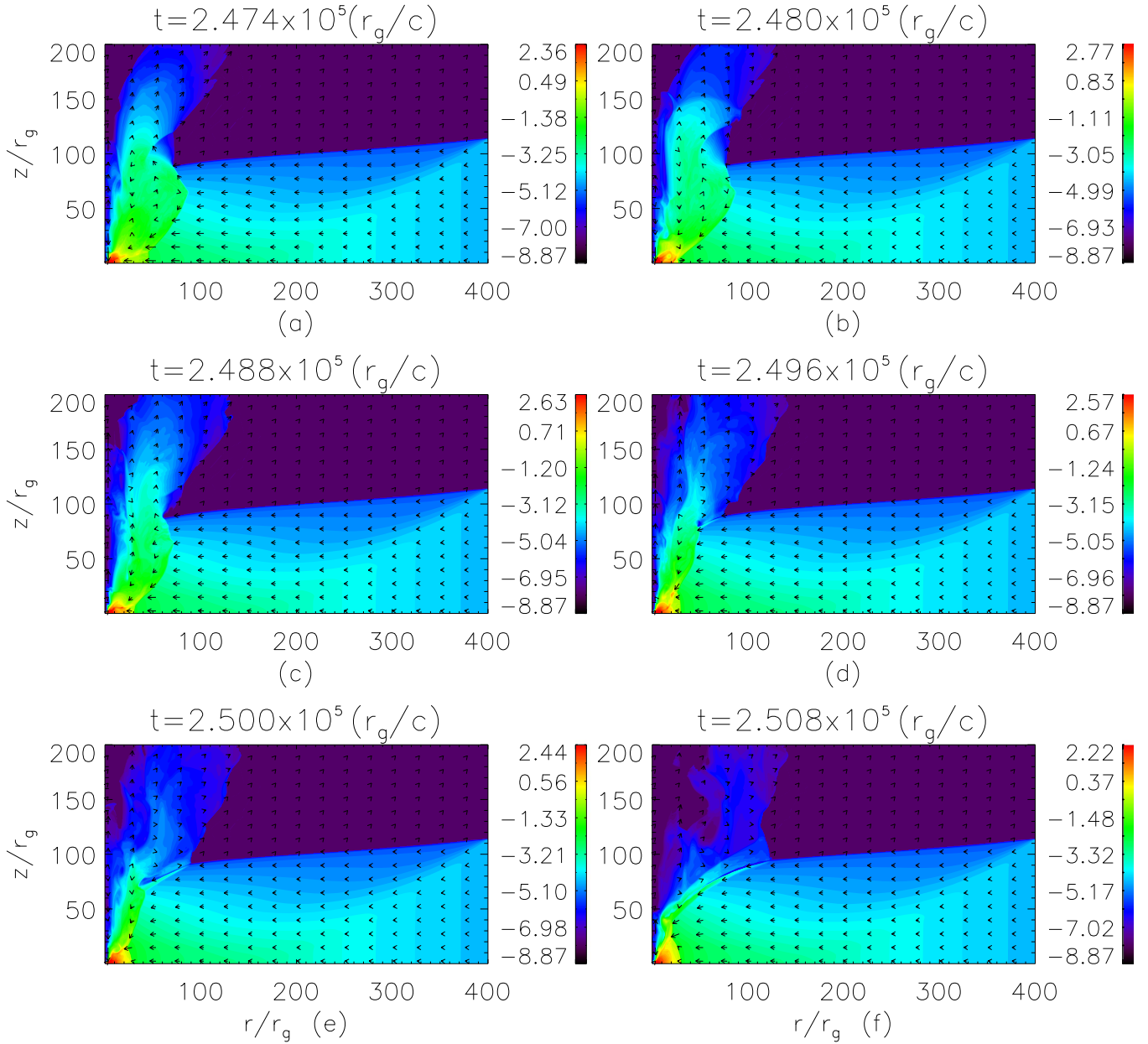
**Figure 10.** Snapshots of density contours and velocity fields in the $r$–$z$ plane for $\alpha = 0.01$. The initial condition is the steady state of M2 and the boundary conditions are same as for M2.

shock flow. Recall that viscosity causes the angular momentum to pile up in the PSD, giving rise to extra centrifugal forces across it, and viscous dissipation also increases the thermal energy. Both effects would push the shock front outward, but as the shock tends to expand, the pressure in the PSD dips, limiting its expansion. Meanwhile, gravity will always attract. Therefore the delicate force balance between all these interactions sets the PSD in oscillation. Since the PSD is an extended dynamical fluid body, the oscillation is, in general, not a simple harmonic one. The shock front while oscillating extends to within 20–50$r_g$ in addition to harboring intermittent inner shocks. One can easily find some smaller period and amplitude oscillations on the top of the larger variety. Oscillations of such large fluid bodies of such a complicated type broaden the power density spectrum, thus reducing the quality (Q) factor of the oscillation.

In Figures 13(a), (c) and (e), we plot $r_{\rm sh}$, $R_{\dot{m}}$ and $\epsilon_{\rm Br}$, for $\alpha = 0.02$, and in Figures 13(b), (d) and (f), we plot $r_{\rm sh}$, $R_{\dot{m}}$, and $\epsilon_{\rm Br}$, respectively, for $\alpha = 0.03$. As the $r_{\rm sh}$ oscillation amplitude increases, the secondary shocks get stronger and the amplitude of $R_{\dot{m}}$ also increases. Interestingly, there is not just one secondary inner shock but also multiple shocks, and the dynamics of these shocks are messy; when an outer shock contracts, the inner one may expand and collide with the incoming outer shock. $R_{\dot{m}}$ also increases from a few percent of the accretion rate to few tens of percent. Since there are many shocks and the outflowing jet interacts with the surface of the accreting material, the dynamics of the shocks are also not regular. The bremsstrahlung emission also follows a similar pattern to that of the shock oscillation.

Figures 14(a), (b) and (c) compare the power spectral density of the radiation emitted by the accreting fluid which harbors
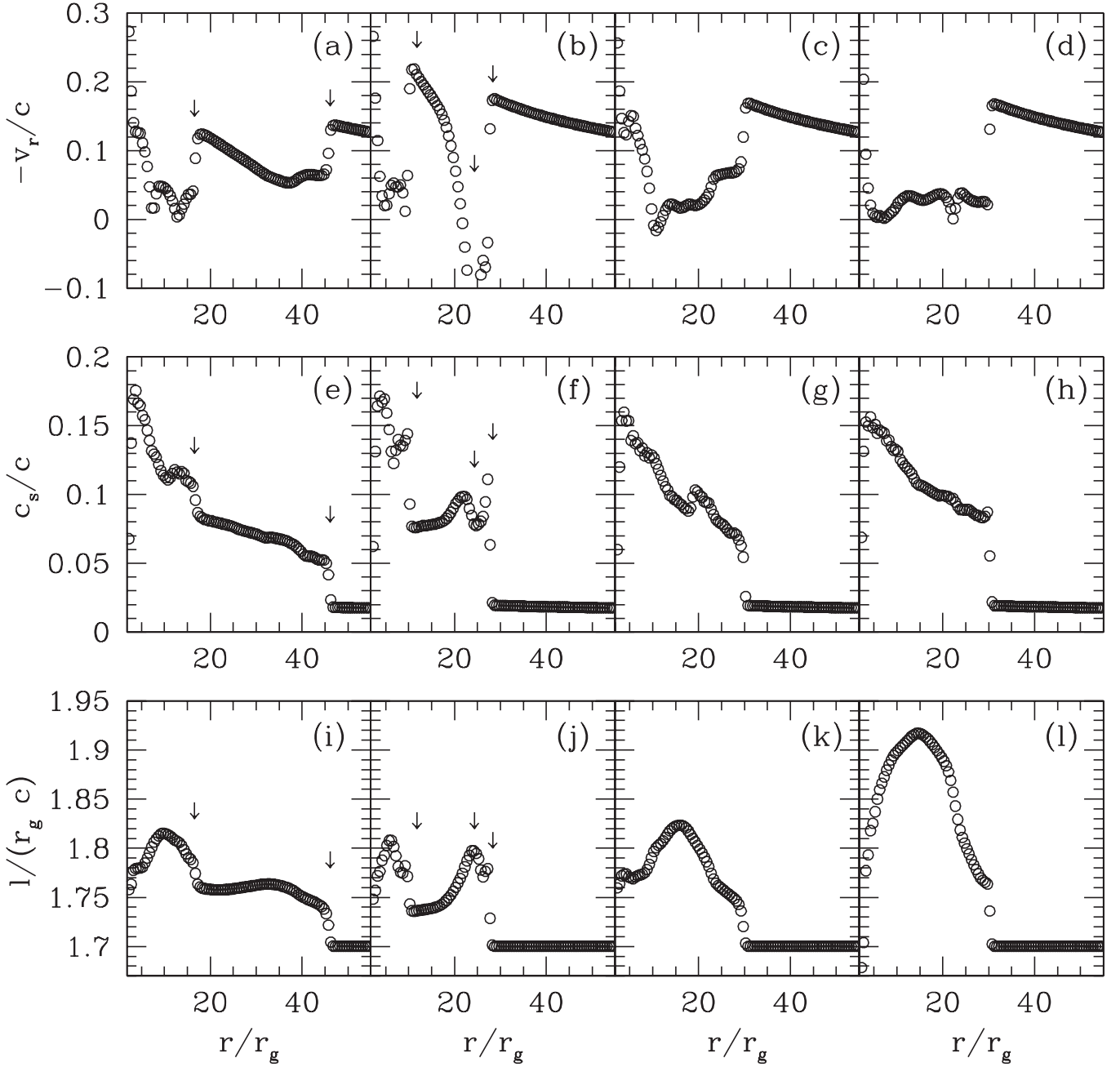
**Figure 11.** Snapshots of $-v_r/c$ (a, b, c, d), $c_s/c$ (e, f, g, h) and $l/(r_g c)$ (i, j, k, l), measured on the equatorial plane, at $t = 2.474 \times 10^5 t_g$ (a, e, i), $t = 2.480 \times 10^5 t_g$ (b, f, j), $t = 2.496 \times 10^5 t_g$ (c, g, k) and $t = 2.508 \times 10^5 t_g$ (d, h, l). The downward arrows show the locations of shocks. The slides indicate the same time snaps as in Figure 10.

oscillating shocks. The presence of multiple shocks, their dynamics, as well as the interaction of the outflowing jet and the accreting matter, makes the shock oscillate irregularly, and hence the power spectral density shows multiple peaks. The outer shock position on average goes from a maximum to a minimum in about $9 \times 10^3 t_g$ for $\alpha = 0.01$, with many small oscillations on the top of it. The period of these small oscillations is about $1500 t_g$. This gives two frequencies of 0.8 Hz and 6.6 Hz if the central black hole is assumed to be of $10\,M_\odot$. Figure 14(a) shows the power density spectrum of the radiation with two peaks. For the case $\alpha = 0.02$, the shock oscillates between $10 r_g$ and $75 r_g$, and $R_{\dot{m}}$ varies from a negligible value to about 10% (Figures 13(a) and (c)). When

increasing the viscosity to $\alpha = 0.03$, $r_{sh}$ oscillates from $10 r_g$ to about $100 r_g$ and the mass outflow rate varies between off-state to more than 20% (Figures 13(b) and (d)). The longer period of shock oscillation for $\alpha = 0.02$ is around $3 \times 10^4 t_g$, and that for $\alpha = 0.03$ is $>3 \times 10^4 t_g$. Assuming $M_B = 10\,M_\odot$, this results in frequencies of 0.3–0.4 Hz (Figures 14(b) and (c)), respectively. But the power density spectrum of the longer period for $\alpha = 0.02$ and 0.03 is almost washed out and resembles a broad hump around 0.3–0.4 Hz. For the three cases shown above, the oscillation of $r_{sh}$ is reflected more clearly from the estimated radiative loss corresponding to the harmonics. For $\alpha = 0.02$ and 0.03, the power density spectra of the estimated radiative loss peak at ~4 Hz and ~3 Hz,
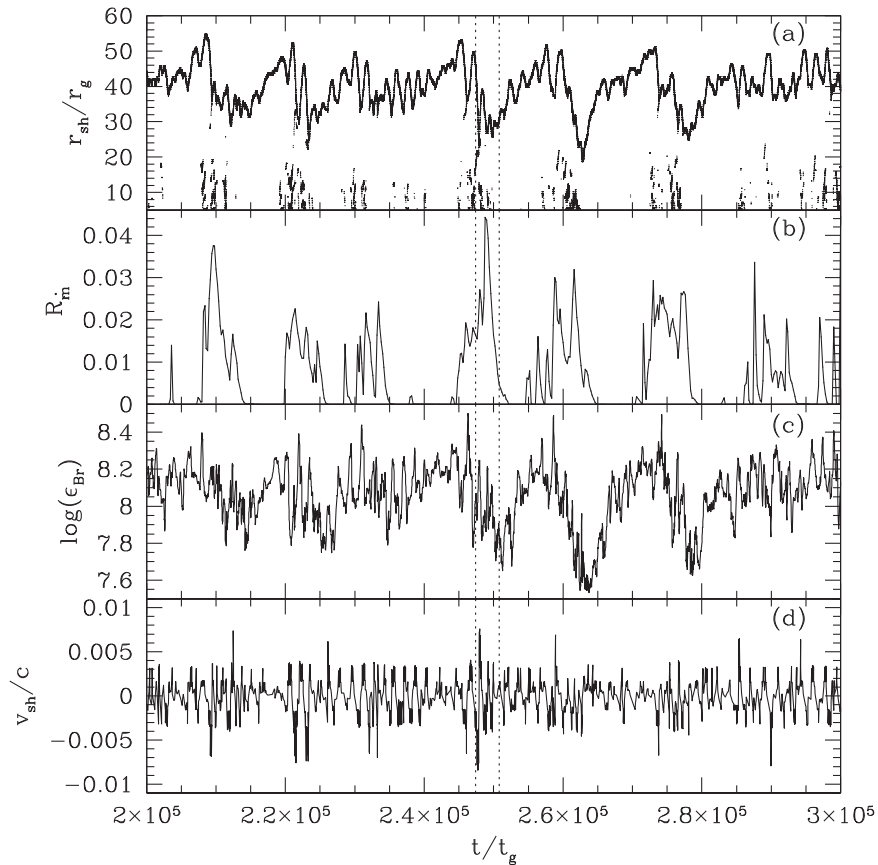
**Figure 12.** Variation of (a) $r_{\rm sh}$, (b) $R_{\dot{m}}$, (c) $\epsilon_{\rm Br}$ bremsstrahlung emission, and (d) shock speed with time. The viscosity is $\alpha = 0.01$, and the snapshots in Figures 10 and 11 are from various times in the rising jet phase depicted within the dotted vertical lines.

respectively. Recall that the PDS is presented in arbitrary units. Smaller periods within a larger period give rise to higher frequencies. It may be noted that, for a low $\alpha$, (i.e., $<0.01$) the median location of the oscillating shock is closer to the horizon, and the period of oscillation is $<10^4 t_g$. So assuming $M_B = 10 M_\odot$, the period obtained is $\lesssim 0.1$ s and the frequency of oscillation is $\gtrsim 10$ Hz. To summarize, increasing $\alpha$ causes a larger-amplitude but lower-frequency shock oscillation for $\alpha < $ few $\times 10^{-2}$, which induces a similar oscillation in the emitted radiation.

### 5.3.1. High-viscosity Parameter

In the literature there have been some multi-dimensional viscous accretion simulations around black holes which harbor accretion shocks (Lanzafame et al. 1998, 2008; Das et al. 2014). As far as we know, all of them were carried out more or less for low-viscosity parameters. With the exception of Lee et al. (2011), most of the simulations were either too hot, or carried out in too small a box size. In order to avoid expensive computation time, simulations were done for an inner few tens of $r_g$ and the boundary conditions were devised in such a way that the shock also forms very close to the horizon. As a result, when the viscosity parameter was increased to $\alpha \gtrsim$ few $\times 10^{-3}$, the shock location escaped the computation box, which led to the conclusion that higher $\alpha$ does not support shocks. However, our work showed that as $\alpha$ is increased, the amplitude of the shock oscillation increases until around $\alpha \sim 0.1$ when $r_{\rm sh}$ goes out of the computational domain, while for $\alpha \sim 0.2$, the oscillation amplitude of the

shock decreases and is within the domain. To illustrate, we plot $-v_r$ (Figures 15(a)–(d)), $c_s$ (Figures 15(e)–(h)) and $l$ (Figures 15(i)–(k)) measured along the equatorial plane, for $\alpha = 0.3$ for the accretion model M2. The time slots are $t = 1.272 \times 10^5$ (a, e, i), $t = 1.276 \times 10^5$ (b, f, j), $t = 1.294 \times 10^5$ (c, g, k) and $t = 1.3 \times 10^5$ (d, h, l). There are clearly two shocks, where the inner moves very close to the horizon at $t = 1.294 \times 10^5$. Higher $\alpha$ ensures more dissipation and therefore higher $c_s$, or, higher temperature (see Figures 15(e)–(h)), which in turn reduces weak multiple inner shocks, and produces two predominant shocks, one inner and the other outer. The inner shock is still intermittent but stronger. More importantly, higher $\alpha$ ensures significant angular momentum reduction even in the pre-shock disk (Figures 15(i)–(k)). Since the accretion shock is primarily centrifugal pressure mediated, lower $l$ near the horizon actually brings the shock back into the computational domain. However, a hotter PSD with higher $\alpha$ creates a very strong gradient in $l$ within it. This ensures a large-amplitude but a relatively shorter-period ($\sim 2800 t_g$) oscillation. As the shock travels to distances $>50 r_g$, the sound speed in the immediate post-shock region is a few times lower than the flow close to the horizon (Figures 15(e)–(h)). This causes more efficient angular-momentum transport in the region closer to the horizon than in the immediate post-shock region, which causes a region of sharp negative gradient of $l$, i.e., $dl/dr < 0$ (see Figure 15(i)). This region of extra centrifugal pressure within the PSD drives the inner shock. The disk model with higher values of $c_s$ and $\alpha$ creates an inner shock, but nonetheless
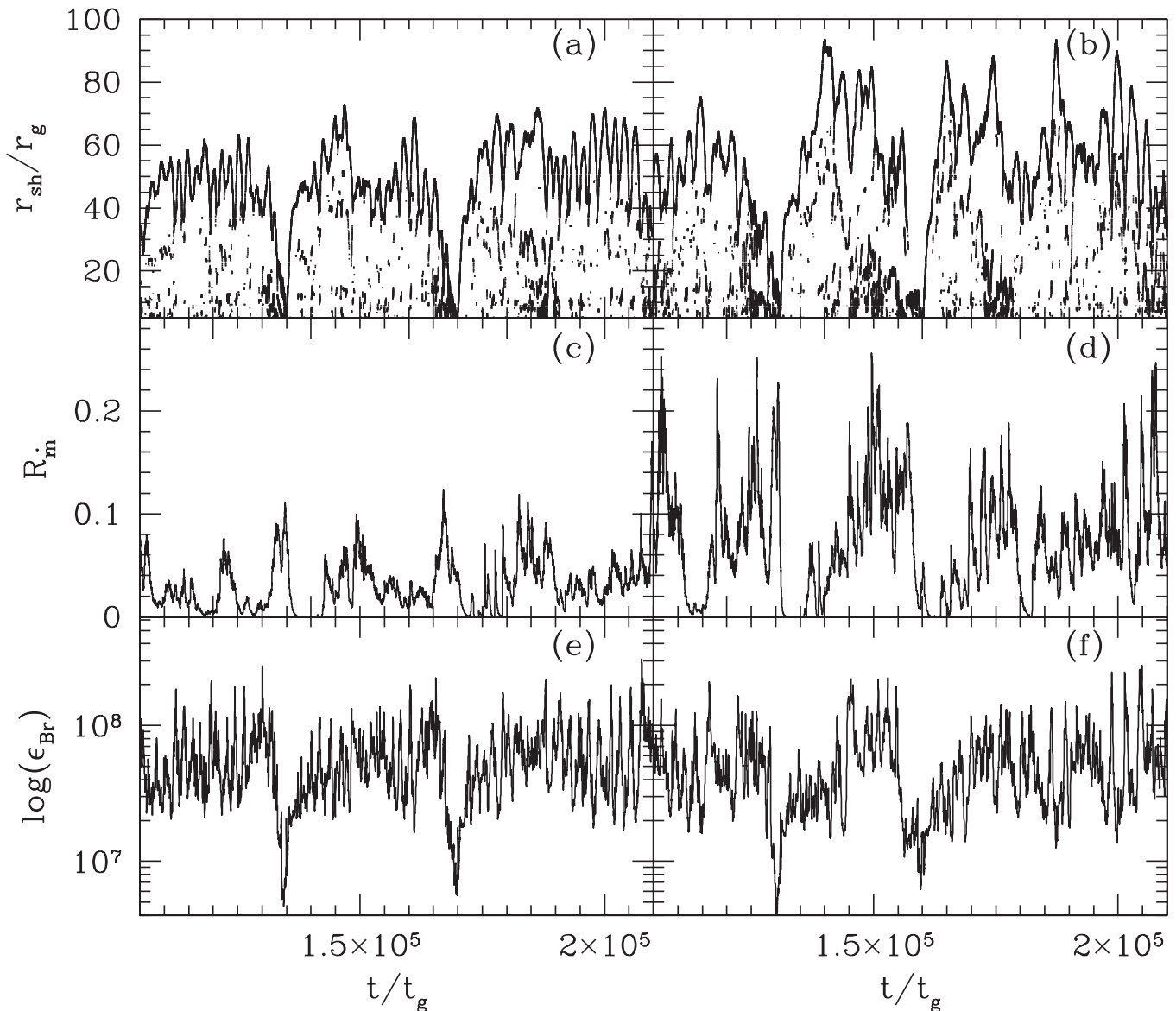
**Figure 13.** Variation of $r_{sh}$ (a, b), $R_{\dot{m}}$ (c, d) and $\epsilon_{Br}$ (e, f) with respect to time for $\alpha = 0.02$ (a, c, e) and $\alpha = 0.03$ (b, d, f). The initial condition is the steady state of M2, and boundary conditions are same as those for M2.

makes the PSD much cleaner than the one for a low $\alpha$. Jets are also much stronger, and therefore jets coming out of the PSD are more collimated than those for lower $\alpha$. A hotter PSD also causes the shock front to expand faster and to trigger a higher-frequency oscillation. Figures 16(a)–(d) show the density contours and velocity vectors in the entire computational domain for the same time slots. These accretion flows form multiple shocks, and at certain times the inner shock may form at the location near the central object as shown in Figure 16(c). It is also clear that the jet is well collimated and fast. Comparison of Figures 10(a)–(f) with Figures 16(a)–(d) shows that the jet in Figures 16(a)–(d) flows much closer to the axis. The angular momentum is vastly reduced due to higher $\alpha$ in Figures 16(a)–(d) making the jet flow closer to the axis. We also plot $c_s$ (Figure 17(a)), $v_z$ (Figure 17(b)) and $\rho$ (Figure 17(c)) with respect to $z$ along the first cell in $r$ ($\equiv$ a distance of $0.5r_g$ from the axis of symmetry); the snapshot of the jet is at $t = 1.198 \times 10^5 t_g$. The velocity profile shows that close to the axis, matter is blown out as a jet (i.e., $v_z > 0$) from

around a height of $30r_g$. The sound speed ($c_s$) decreases with height, while velocity increases, making the jet supersonic and eventually it undergoes a series of shocks. The jet speed is fairly high ($\sim 0.2c$) especially when the distance is $\sim 200r_g$ which is not a distance at which one expects a jet to reach its terminal speed. Interestingly, the jet velocity profile (Figure 17(b)) also does not reach an asymptotic value and continues to increase at $z = 200r_g$.

In the following, we compare various properties of flows starting with the same injection parameters, and with two different but high values of $\alpha$. Figures 18(a) and (b) show $r_{sh}$ with time, while in Figures 18(c) and (d) we show the compression ratio $v_-/v_+$, and in Figures 18(e) and (f), $R_{\dot{m}}$ with respect to time. In Figures 18(g) and (h), we plot the power density spectrum (in arbitrary units) of the radiation emitted by the flow. Figures 18(a), (c), (e), (g), are plotted for viscosity $\alpha = 0.2$ and Figures 18(b), (d), (f), (h), are plotted for $\alpha = 0.3$. Figures 18(a) and (b) show the median of the oscillating shock that has formed closer to the central object as $\alpha$ is increased
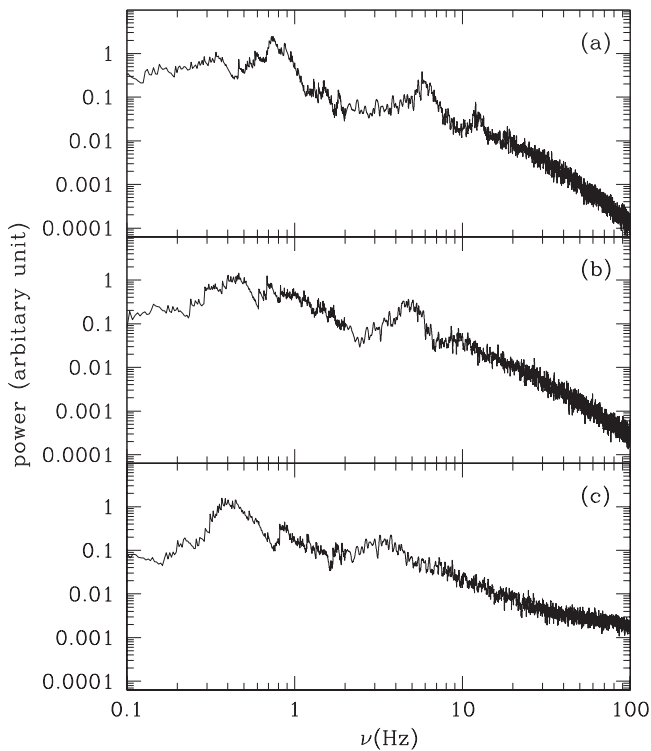
**Figure 14.** Comparison of the power spectral density (arbitrary units) transform of the shock oscillation for $\alpha = 0.01$ (a), $\alpha = 0.02$ (b), and $\alpha = 0.03$ (c). The spectral density is obtained considering a stellar mass BH of $M_{\mathrm{BH}} = 10 M_\odot$.

from $0.2 \rightarrow 0.3$. The compression ratio of the oscillating shock may far exceed the steady-state values. However, in the case of $\alpha = 0.3$, the compression ratio is obviously higher because the median of the shock is located closer to the black hole. The corresponding mass outflow rate for $\alpha = 0.3$ is slightly higher than that for $\alpha = 0.2$. If the shock is located closer to the inner zone, then the frequency of oscillation should also be higher. For $\alpha = 0.3$ the frequency of oscillation is around 4 Hz, while for $\alpha = 0.2$ it is $\sim$3.5 Hz. Although both peaks are broad, the peak for $\alpha = 0.2$ is comparatively broader. The quality factor of the peaks in the power density spectra are $\sim$2 for $\alpha = 0.2$ and $\sim$3 for $\alpha = 0.3$. It is interesting to note that for a viscosity of $\alpha \lesssim \mathrm{few} \times 10^{-2}$, the shock expands with increasing $\alpha$, while for $\alpha \sim \mathrm{few} \times 0.1$, the trend is the opposite. We will discuss this in the next section.

## 6. SUMMARY AND DISCUSSION

In this paper, we simulated the evolution of an advective, viscous accretion disk. But instead of randomly chosen values of injected flow variables, we adopted values from the analytical solutions of Kumar & Chattopadhyay (2013). The excellent agreement of the simulation results with the analytical results when they achieved the steady state shows that the analytical results are indeed steady, and that the numerical code is also very robust. We extended the algorithm of our one-dimensional code (Lee et al. 2011) to multi-dimensions. We regenerated and compared shocked and shock-free steady-state viscous solutions with those from Kumar & Chattopad-hyay (2013). We considered a shock-free inviscid solution and a shocked inviscid solution corresponding to two different boundary conditions (referred to as cases M1 and M2), and varied $\alpha$ to obtain steady-state as well as time-dependent

solutions. Note that even without any given artificial shock conditions, the shock conditions are inbuilt as in any upwind code, as these codes are based on conservation laws of flow variables which ensure sharp reproduction of shocks. Since in each cell all the fluxes are conserved, automatically shocks arise if the preferred conditions prevail in the flow. Such a shock admits entropy and a temperature jump across the shock front. In an ideal fluid this gives rise to the Rankine–Hugoniot jump conditions across the shock front. Such a shock results in higher entropy, and a higher density post-shock flow, whereas the velocity is smaller. Such hotter, slower, denser regions are susceptible to various dissipative processes and are radiatively more efficient than the pre-shock flow.

We found that the low angular momentum, shock-free accretion becomes similar to a Bondi flow in the presence of viscosity. No jet-like flow developed when viscosity was turned on for the shock-free accreting flow with the initial conditions of case M1. However, turning on the viscosity for the shocked accretion flow with the initial conditions of case M2, the shock persists in the steady state for lower values of $\alpha$, but starts to oscillate at higher $\alpha$. Looking closer, one finds that a hotter PSD transports angular momentum more efficiently than the colder pre-shock disk (see Equations (3) and (8)). As a result, the angular momentum distribution becomes steeper in the PSD than in the pre-shock disk, causing an extra centrifugal force on the shock front to push it out, but the sum of ram pressure and gas pressure of the outer disc would oppose the expansion. The net effect is that, for small $\alpha$, the accretion shock settles down to a steady value. But above a certain critical viscosity parameter ($\alpha_{\mathrm{cr}}$), the shock starts to oscillate, and the mass outflow in the form of bipolar jets increases in strength. In the particular case of M2, $\alpha_{\mathrm{cr}} = 0.003$. As $\alpha > \alpha_{\mathrm{cr}}$, the shock initially undergoes small perturbations but on increasing $\alpha$ the shock undergoes small-amplitude regular oscillations. With even larger $\alpha$, the oscillation amplitude increases, and the oscillation itself becomes irregular. There are multiple factors in play: the PSD will expand less toward the incoming pre-shock supersonic flow than in the vertical direction. In fact, the extra thrust of the oscillating PSD ejects matter in episodes along the vertical direction. The mass that is being ejected might interact with the infalling matter at the interface, which gives rise to a different kind of perturbation. Moreover, as $r_{\mathrm{sh}}$ moves out to large distance, the angular momentum transport within the PSD becomes complicated. The flow near the horizon is much hotter than that near the expanding shock front. This causes the angular momentum distribution in the PSD to change, from a slow monotonic rise of $l$ peaking at some value when $r_{\mathrm{sh}}$ is small, to, two or more sharp peaks when $r_{\mathrm{sh}}$ is large. This causes multiple shocks to form (see Lee et al. 2011 for details of multiple shocks). All of these cause irregular oscillation of shocks and, because of the irregularity, power density spectra of the shocks show broader peaks than when the oscillation is more regular (Das et al. 2014).

According to Das et al. (2014), the mass outflow for small-amplitude regular oscillations is episodic and the period of the episodic mass loss matches that of the shock oscillation. Their results also showed the existence of one or a few sharp peaks in the power spectrum of the shock, as well as of the estimated radiation from the flow. We checked the case of $=0.005$ (Figure 9(b)) which also exhibits regular oscillation, and shows a sharp fundamental peak ($\gtrsim$10 Hz) with higher harmonics

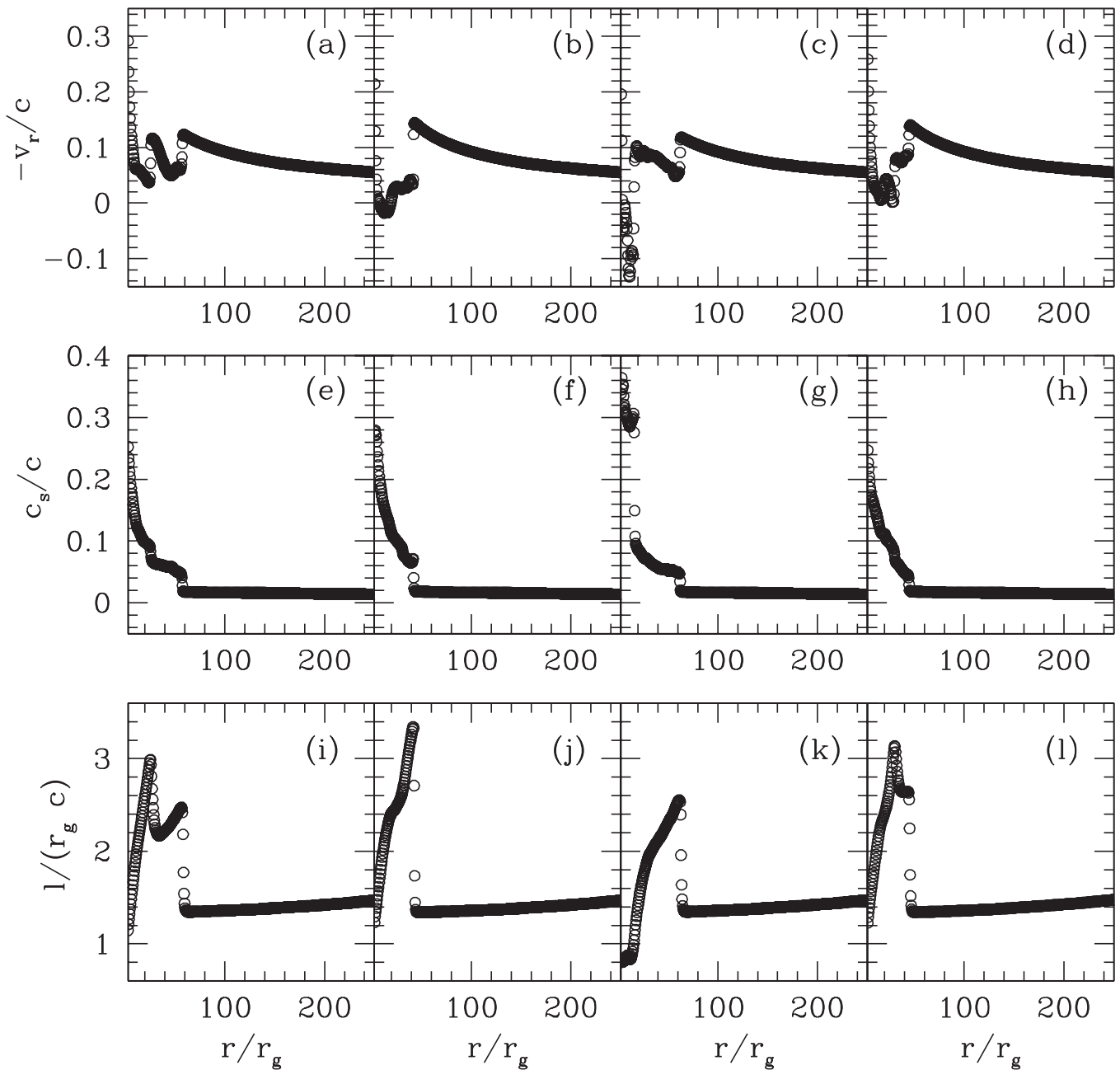**Figure 15.** Snapshots of $-v_r$ (a, b, c, d), $c_s$ (e, f, g, h) and $l$ (i, j, k, l) measured in geometrical units, and evaluated on the equatorial plane. The various time snapshots are at $t = 1.272 \times 10^5$ (a, e, i), $t = 1.276 \times 10^5$ (b, f, j), $t = 1.294 \times 10^5$ (c, g, k), and $t = 1.3 \times 10^5$ (d, h, l). The viscosity parameter $\alpha = 0.3$ and initial condition is the steady state of M2 and the boundary conditions are also identical to those for M2.

somewhat similar to those of Das et al. (2014). Although the fundamental frequency of oscillation was lower for the boundary condition of Das et al. (2014), note that they performed a simulation for a comparatively hotter, lower angular momentum flow. In the present case, the flow is colder but of higher angular momentum. Therefore, apart from the location of the shock, the flow properties across it also affect the QPO frequency.

For irregular large-amplitude shock oscillations, we compared the time evolution of mass loss with the shock oscillation, and showed that as the shock front starts to contract, it squeezes more matter in the vertical direction, but as it expands from the $r_{sh}$ minimal position, the PSD loses the upward thrust and the mass outflow collapses, generating the

episodic mass outflow. We note that there is a significant interval of literally no outflow which corresponds to a jet "off" state. We also confirm that during the steady state, the mass outflow rate from the PSD is either absent or weak. Only when the shock activity becomes intensified, and thereby the PSD oscillates appreciably, does the mass outflow rate increase. As the viscosity is increased, the shock oscillation amplitude increases, which triggers a large amount of mass ejection in the form of jets. The fundamental oscillation period also increases, and the PSD has a messy structure with many intermittent secondary shocks. This pattern tends to continue for a disk with $\alpha < 0.1$. For $\alpha = 0.1$, the oscillation amplitude increases to an extent that it actually exceeds the computational domain. But interestingly, for $\alpha \geqslant 0.2$, the shock oscillation becomes
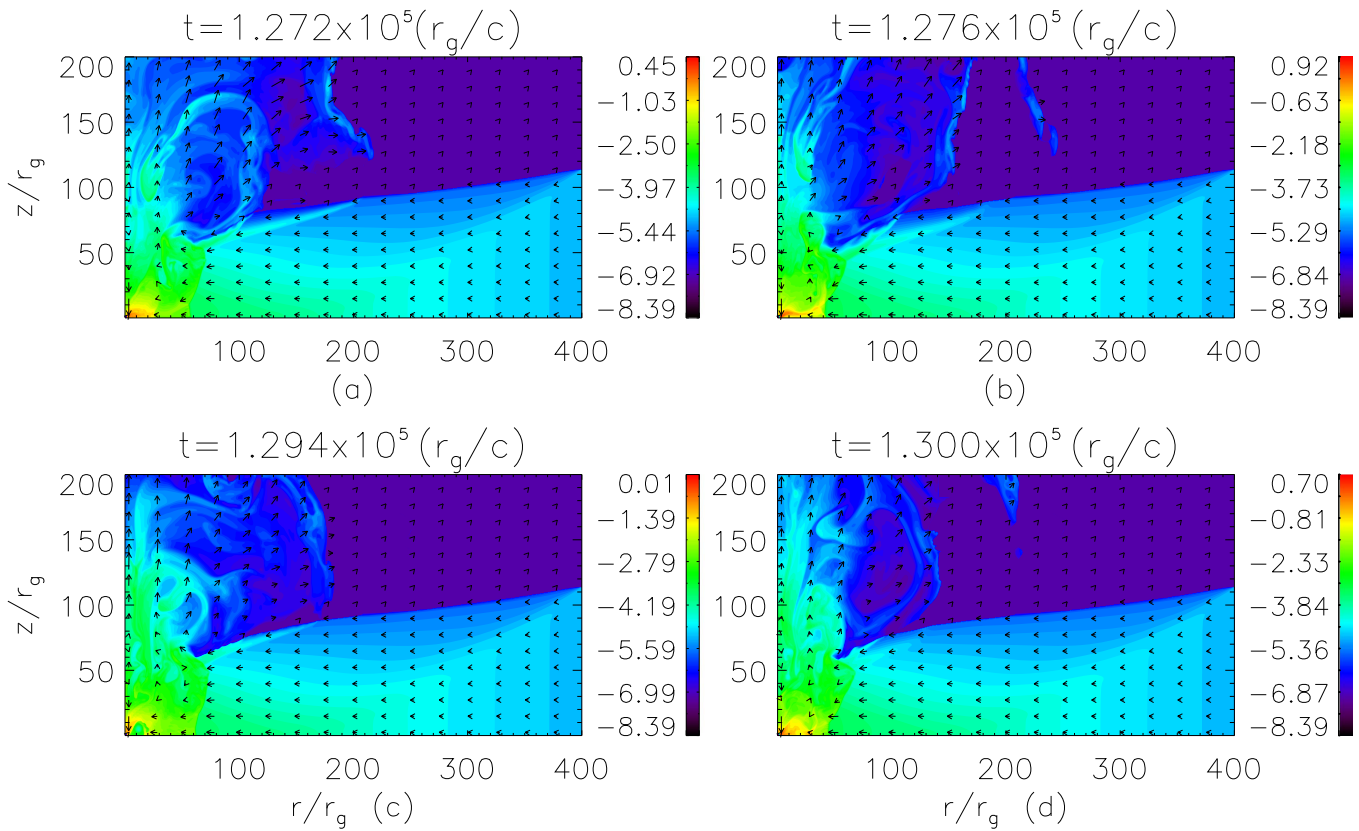
**Figure 16.** Contours of density and velocity vectors of an accretion disk and its jet. The various time snaps are at $t = 1.272 \times 10^5, 1.276 \times 10^5, 1.294 \times 10^5$, and $1.3 \times 10^5$. The viscosity parameter is $\alpha = 0.3$, and is the complete solution of Figure 15.

confined within the computational box and the frequency of oscillation increases. Therefore, our simulation results show that for a lower range of viscosity, i.e., $\alpha \sim$ few $\times 10^{-2}$, the median of the oscillating shock increases with $\alpha$, while in the range of $0.1 < \alpha \lesssim$ few $\times 0.1$, the median of the shock location decreases with increasing $\alpha$! The question is: why is this so?

Recently, Kumar & Chattopadhyay (2013, 2014) showed for a variety of equations of state of the accretion disk fluid that $r_{sh}$ decreases with increasing $\alpha$ if the flow starts from the same outer boundary conditions. The explanation for such behavior is that a higher $\alpha$ causes a higher angular momentum transport, reducing the pre-shock angular momentum of the disc, causing $r_{sh}$ to shift closer to the horizon. Kumar & Chattopadhyay (2013), in particular, also showed that the cause of the shock expansion with increasing $\alpha$ in various simulations (including our previous paper, Lee et al. 2011) is the short boundary considered for most simulations. By "short" we do not mean a particular fixed value, but one that actually varies depending on the flow parameters. For some flow parameters, the angular momentum achieves its local Keplerian value at a distance of a few $\times 100r_g$, while for others, $l = l_K$ is achieved at a distance of $\sim 10^5 r_g$. Therefore a computational box of a few $\times 100r_g$ is adequate for the former case, but will be considered "short" for the latter case (see, e.g., Figures 5(d), (e) of Kumar & Chattopadhyay 2013).

Viscosity is more effective for a hotter and slower flow as seen in Equation (22). Hence, viscosity is more effective in the PSD than the colder pre-shock disk. If the outer boundary is short, then $\alpha$ cannot significantly affect the flow properties in the pre-shock disk, but efficiently transports angular momentum in the PSD. This causes the angular momentum to pile up in the PSD, while in the pre-shock disk $l$ has a low gradient and, as a result, the shock front expands in order to negotiate the increased centrifugal force. As we increase $\alpha$, more angular momentum will be piled up in the PSD, but the flow properties in the pre-shock disk will largely remain unaffected, and the shock would expand further. This is roughly what is expected for lower $\alpha$ as shown in our simulations. Moreover, as the shock becomes oscillatory, for similar reasons, both the median shock location and the oscillation amplitude increase with increasing $\alpha$. This also causes the emitted radiation to oscillate with decreasing frequency when $\alpha$ is increased. Why is this trend reversed for higher $\alpha$ (e.g., Figure 18)?

The computational box of $400r_g$, though larger than most simulation set-ups, is still much smaller compared to the actual size of the theoretical accretion disk (see Figures 7(a)–(c) for comparison). To understand the situation, let us first focus on Figure 7, where we compared the steady-state numerical solution with the analytical one for the same values of $v_r$(inj), $c_s$(inj), $l_{inj}$ at $r_{inj}$. It is clear that $r_{inj}$ is not the actual outer boundary ($10^5 r_g$). For low $\alpha$, the angular momentum at the outer boundary will be $l|_{r=10^5 r_g} \gtrsim l_{inj}$. As we increase $\alpha$, for the same injected values at the same $r_{inj}$, $l$ at $r = 10^5 r_g$ will be larger and for some value of $\alpha = \alpha_k$, $l$ will attain its Keplerian ($l_K = r^{3/2}/[\sqrt{2}\,(r-1)]$) value at $10^5 r_g$. Then for any $\alpha > \alpha_k$, the $l$ distribution will attain its Keplerian value at a distance shorter than $10^5 r_g$. Note that for advective–transonic disks, the boundary at which the disk attains $l = l_K$ has to be the maximum value of its outer boundary. For $\alpha \lesssim$ few $\times 0.01$,
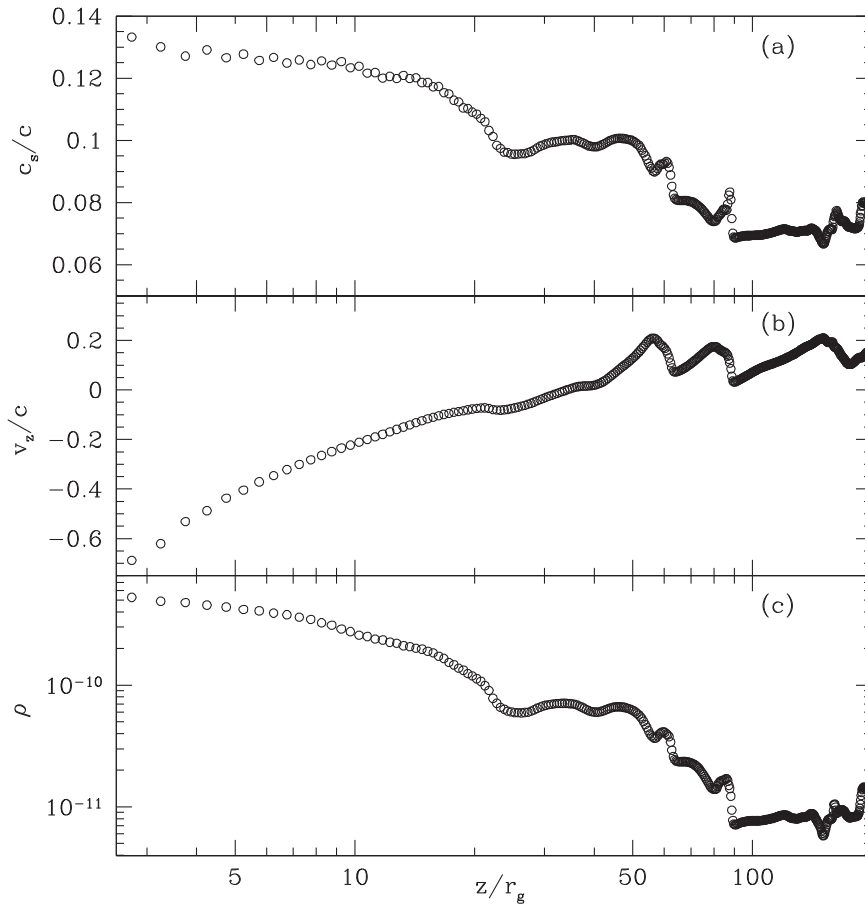
**Figure 17.** Jet profile plotted along the $z$ coordinate during the "jet on state" at $t = 1.198 \times 10^5 t_g$ for the same case as Figure 15; the sound speed (a), $v_z$ (b), and density $\rho$ (c). The flow variables plotted are taken from the first cell adjacent to the axis.

i.e., small $\alpha$, $l$ does not attain $l_K$ within $10^5 r_g$. But for $\alpha \sim$ few $\times$ 0.1 the outer boundary effectively comes closer, simply because we have kept the injection parameters constant. By the same token, $l$ will be substantially reduced as we go inward from $r_{inj}$ up to $r_{sh}$ (for details, see Figure 5 of Kumar & Chattopadhyay 2013), causing the shock position to relocate closer to the central object. So although $r_{inj} = 400 r_g$ is still properly not the outer boundary, for $\alpha \sim$ few $\times$ 0.1, the same $r_{inj}$ is closer to the outer boundary, therefore "mimicking" the fact that with the increase of $\alpha$, the shock moves closer to the central object. Meanwhile, for $\alpha \lesssim$ few $\times$ 0.01, $r_{inj}$ is nowhere close to the real outer boundary. This is the reason why we see $r_{sh}$ increasing with $\alpha$ for the range of a $\alpha <$ few $\times 10^{-2}$, but $r_{sh}$ decreasing with increasing $\alpha$ for $\alpha \gtrsim$ few $\times$ 0.1. The bottom line is that in simulation boxes with a short boundary, we are actually comparing accretion flows with different outer boundary conditions, where incidentally for a small range of higher $\alpha$, $r_{inj}$ somewhat mimics the outer boundary.

The mass outflow rate for higher $\alpha$ appears to be sporadic, with inconspicuous jet "off" states. Since the viscosity is very strong for $\alpha = 0.3$, a higher viscous dissipation and more significant angular momentum transport induce a higher-frequency shock oscillation. The jet becomes much stronger at $\alpha = 0.3$, to the extent that the average jet speed near the axis is $\sim 0.2c$ at a height of $200 r_g$ above the equatorial plane. One may wonder whether we should call these outflows jets, given the fact that they are not truly relativistic. We note two points in the jet characteristics. First, jets are collimated ejections.

Figures 10 and 16 clearly show that the outflow is fairly collimated (the bulk of it is spread within $100 r_g$ at a height of $200 r_g$). Next, these outflows leave the computational domain at $v \sim 0.2c$, which is mildly relativistic and clearly transonic (Figures 17(a) and (b)). So according to these conditions, they qualify as jets. From Figure 17(b), the jet is obviously not reaching its asymptotic value at the height of $200 r_g$; therefore a somewhat higher speed can be expected at $z > 200 r_g$. However, this is not an indication that this jet will go on to reach a relativistic terminal speed. One must also bear in mind that not all jets, especially those around micro-quasars, are always truly relativistic (S433; Margon 1984, and the 2009 burst of H1743-22; Miller-Jones et al. 2012). Our simulation set-up does not address the transition from intermediate states to the high-soft state (or transitions across the jet line) and the associated ejection of relativistic blobs. We simulate the origin of semi-relativistic jets associated with the low-hard state and the intermediate states. And indeed such jets increase in strength as the BHCs move from low-hard to intermediate-hard spectral states (Fender et al. 2004).

In various papers, many authors have shown that in outbursting sources low QPO frequencies emerge in the hard states and increases as the object transits from low-hard states to the intermediate states. Such a QPO is not detected during the ejection of relativistic jets (Casella et al. 2004; McClintock & Remillard 2006; Nandi et al. 2012). In the model, the shock being situated at large distances is equivalent to a low-hard state, and as the median of the oscillating shock moves toward
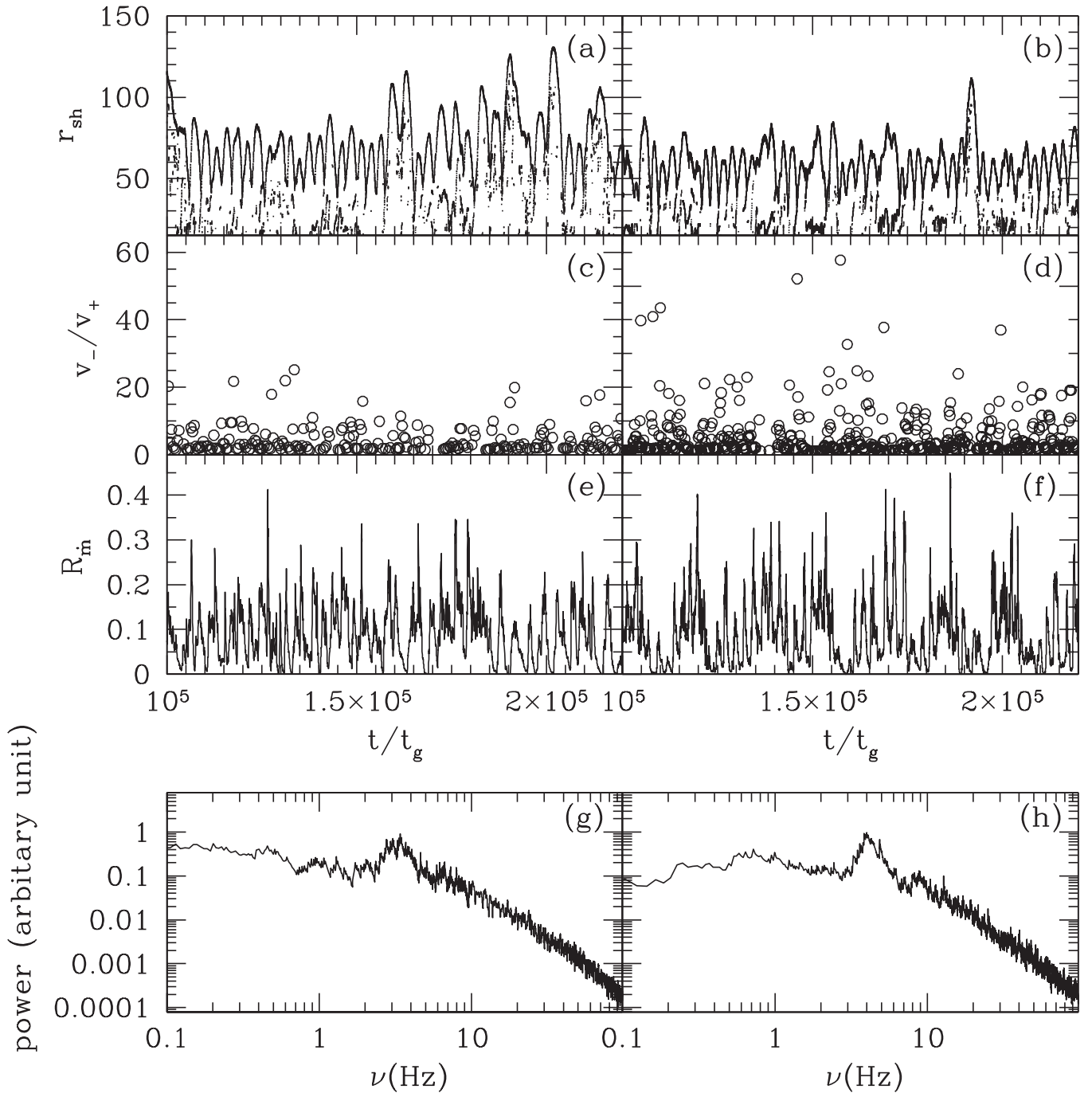
**Figure 18.** Variation of $r_{sh}$ (a, b), compression ratio $v_-/v_+$ (c, d), $R_{\dot{m}}$ (e, f) with time. The power density spectrum in arbitrary units (g, h) for the two viscosity cases are plotted vs. frequency. The left panels (a, c, e, g) represent flow with $\alpha = 0.2$ and the right panels (b, d, f, h) represent flow with $\alpha = 0.3$. The boundary conditions are same as for M2.

the central object, the total disk luminosity increases. Any perturbation of the shock, while as a whole moving toward the central object, would increase the frequency of the oscillation. Simultaneously, the mildly relativistic jet becomes stronger (Q diagram of Fender et al. 2004), as also seen in our simulation. Although we could not track its entire evolution because of the limitation of the simulation box size, at least for higher $\alpha$, the increase of the QPO frequency and strengthening of the mildly relativistic jets somewhat justify the theoretical conjecture (Kumar & Chattopadhyay 2013, 2014; Chattopadhyay & Kumar 2016). However, the whole set of state transitions can

emerge if and only if one simulates an accretion flow from the actual outer boundary (where $l = l_K$, or, $r_{inj} = 10^5 r_g$) and higher $\alpha$, which is very challenging to achieve and currently beyond the scope of this paper.

There have been other interesting investigations in the advective flow regime, for instance, general relativistic hydrodynamic simulations (Nagakura & Yamada 2009) and investigations of transmagnetosonic flow in general relativity (Takahashi et al. 2002, 2006; Fukumura et al. 2007). While Nagakura & Yamada (2009) only simulated inviscid flow and reported a shock oscillation of a few Hz, the main realization

was that it is possible to obtain steady and oscillatory shocks in general relativistic simulations. Transmagnetosonic flow also revealed the formation of general relativistic MHD shocks. The presence of both slow and fast MHD shocks opens up hitherto uncharted possibilities. Fast shocks may generate transverse magnetic fields, which can help in powering jets. An interesting investigation may be taken up to identify various spectral states with MHD-type shocks.

We conclude that a shocked accretion disk through the oscillation of the PSD naturally explains the QPO phenomenon in BHCs, while an episodic jet seems to become stronger as viscosity increases. For weak viscosity the jet is also weaker, while an oscillating shock due to its "bellows action" is squeezing out episodic jets at fairly high speed. In Lee et al. (2011), the median shock location was large and therefore the frequency of oscillation obtained was around 0.1 Hz, whereas in Das et al. (2014), the median shock location was at a few $\times$ 10 $r_g$. In addition, the frequency was around a few Hz. In this paper, we investigated a large range of viscosity parameters but starting with the same initial condition, and we were able to generate frequency ranges from less than one to a few Hz. Moreover, Lee et al.'s (2011), analysis, being one-dimensional, failed to simulate shock oscillation beyond $\alpha > 0.1$, but following their conjecture, we show that the formation of jet/outflows in multi-dimensional simulations saturates the shock oscillation for higher $\alpha$ and retains it within the computational domain, where it is shown that a transient shock survives even with high viscosity parameters, and the mass outflow rate also becomes stronger for such a flow.

## REFERENCES

Becker, P. A., Das, S., & Le, T. 2008, ApJL, 677, L93
Casella, P., Belloni, T., Homan, J., & Stella, L. 2004, A&A, 426, 87
Chakrabarti, S. K. 1989, ApJ, 347, 365
Chakrabarti, S. K. 1996, ApJ, 464, 664
Chakrabarti, S. K., & Titarchuk, L. 1995, ApJ, 455, 623
Chattopadhyay, I., & Chakrabarti, S. K. 2011, IJMPD, 20, 1597
Chattopadhyay, I., & Das, S. 2007, NewA, 12, 454
Chattopadhyay, I., & Kumar, R. 2016, MNRAS, 459, 3792
Chattopadhyay, I., & Ryu, D. 2009, ApJ, 694, 492
Chen, X., Abramowicz, M., & Lasota, J.-P. 1997, ApJ, 476, 61
Das, S., Chattopadhyay, I., Nandi, A., & Molteni, D. 2014, MNRAS, 442, 251
Fender, R. P., Belloni, T. M., & Gallo, E. 2004, MNRAS, 355, 1105
Fukue, J. 1987, PASJ, 39, 309
Fukumura, K., Takahashi, M., & Tsuruta, S. 2007, ApJ, 657, 415
Fukumura, K., & Tsuruta, S. 2004, ApJ, 611, 964
Gallo, E., Fender, R. P., & Pooley, G. G. 2003, MNRAS, 344, 60
Giri, K., & Chakrabarti, S. K. 2013, MNRAS, 430, 2836
Gu, W. M., & Foglizzo, T. 2003, A&A, 409, 1
Gu, W. M., & Lu, J. F. 2002, ChA&A, 26, 147
Gu, W. M., & Lu, J. F. 2006, MNRAS, 365, 647
Harten, A. 1983, JCoPh, 49, 357
Hsieh, H. S., & Spiegel, E. A. 1976, ApJ, 207, 244
Junor, W., Biretta, J. A., & Livio, M. 1999, Natur, 401, 891
Kato, S., Fukue, J., & Mineshige, S. 1998, Black-hole Accretion Disks (Kyoto: Kyoto Univ. Press)
Kumar, R., & Chattopadhyay, I. 2013, MNRAS, 430, 386
Kumar, R., & Chattopadhyay, I. 2014, MNRAS, 443, 3444
Kumar, R., Chattopadhyay, I., & Mandal, S. 2014, MNRAS, 437, 2992
Kumar, R., Singh, C. B., Chattopadhyay, I., & Chakrabarti, S. K. 2013, MNRAS, 436, 2864
Lanzafame, G., Cassaro, P., Schilliró, F., et al. 2008, A&A, 482, 473
Lanzafame, G., Molteni, D., & Chakrabarti, S. K. 1998, MNRAS, 299, 799
Lee, S.-J., Ryu, D., & Chattopadhyay, I. 2011, ApJ, 728, 142
Liang, E. P. T., & Thompson, K. A. 1980, ApJ, 240, 271L
Lu, J. F., Gu, W. M., & Yuan, F. 1999, ApJ, 523, 340
Mandal, S., & Chakrabarti, S. K. 2010, ApJL, 710, L147
Margon, B. 1984, ARA&A, 22, 507
McClintock, J. E., & Remillard, R. A. 2006, in Compact Stellar X-ray Sources, ed. W. H. G. Lewin & M. van der Klis (Cambridge: Cambridge Univ. Press)
Michel, F. C. 1972, Ap&SS, 15, 153
Mihalas, D., & Mihalas, B. W. 1984, Foundations of Radiation Hydrodynamics (Oxford: Oxford Univ. Press)
Miller-Jones, J. C. A., Sivakoff, G. R., Altamirano, D., et al. 2012, MNRAS, 421, 468
Miyamoto, S., Kitamoto, S., Iga, S., Negoro, H., & Terada, K. 1992, ApJ, 391, 21
Molteni, D., Lanzafame, G., & Charkrabarti, S. K. 1994, ApJ, 425, 161
Molteni, D., Ryu, D., & Chakrabarti, S. K. 1996a, ApJ, 470, 460
Molteni, D., Sponholz, H., & Chakrabarti, S. K. 1996b, ApJ, 457, 805
Molteni, D., Tóth, G., & Kuznetsov, O. A. 1999, ApJ, 516, 411
Morgan, E. H., Remillard, R. A., & Greiner, J. 1997, ApJ, 482, 993
Nagakura, H., & Yamada, S. 2009, ApJ, 696, 2026
Nakayama, K. 1992, MNRAS, 259, 259
Nakayama, K. 1994, MNRAS, 270, 871
Nandi, A., Debnath, D., Mandal, S., & Chakrabarti, S. K. 2012, A&A, 542, 56
Narayan, R., Kato, S., & Honma, F. 1997, ApJ, 476, 49
Nobuta, K., & Hanawa, T. 1994, PASJ, 46, 257
Novikov, I. D., & Thorne, K. S. 1973, in Black Holes, ed. B. S. Dewitt & C. Dewitt (New York: Gordon and Breach), 343
Okuda, T., Teresi, V., & Molteni, D. 2007, MNRAS, 377, 1431
Paczyński, B., & Wiita, P. J. 1980, A&A, 88, 23
Press, W. H., Teukolsky, S. A., Vetterling, W. T., & Flannery, B. P. 1992, Numerical Recipes in Fortran (New York: Cambridge Univ. Press)
Radhika, D. A., & Nandi, A. 2014, AdSpR, 54, 1678
Remillard, R. A., & McClintock, J. E. 2006, ARA&A, 44, 49
Remillard, R. A., Muno, M. P., McClintock, J. E., & Orosz, J. A. 2002a, ApJ, 580, 1030
Remillard, R. A., Sobczack, G. J., Muno, M. P., & McClintock, J. E. 2002b, ApJ, 564, 962
Ryu, D., Brown, G. L., Ostriker, J. P., & Loeb, A. 1995a, ApJ, 452, 364
Ryu, D., Chakrabarti, S. K., & Molteni, D. 1997, ApJ, 474, 378
Ryu, D., Ostriker, J. P., Kang, H., & Cen, R. 1993, ApJ, 414, 1
Ryu, D., Yun, H. S., & Choe, S.-U. 1995b, JKAS, 28, 223
Shakura, N. L., & Sunyaev, R. A. 1973, A&A, 24, 337
Shapiro, S. L. 1973a, ApJ, 180, 531
Shapiro, S. L. 1973b, ApJ, 185, 69
Shapiro, S. L., & Teukolsky, S. A. 1983, Black Holes, White Dwarfs and Neutron Stars, Physics of Compact Objects (New York: Wiley-Interscience)
Strang, G. 1968, SJNA, 5, 505
Sunyaev, R. A., & Titarchuk, L. 1980, A&A, 86, 121
Takahashi, M., Goto, J., Fukumura, K., Rillet, D., & Tsuruta, S. 2006, ApJ, 645, 1408
Takahashi, M., Rillet, D., Fukumura, K., & Tsuruta, S. 2002, ApJ, 572, 950
Vyas, M. K., Kumar, R., Mandal, S., & Chattopadhyay, I. 2015, MNRAS, 453, 2992